Advances in Optics and Photonics

Recent advances in plasmonic photonic crystal fibers: design, fabrication and applications

Dora Juan Juan Hu[1,*] and Ho Pui Ho[2]

[1]*Institute for Infocomm Research, Singapore, Singapore*
[2]*Department of Electronic Engineering, The Chinese University of Hong Kong, Hong Kong SAR, China*
Corresponding author: jjhu@i2r.a-star.edu.sg

Flexibility in engineering holey structures and controlling the wave guiding properties in photonic crystal fibers (PCFs) has enabled a wide variety of PCF-based plasmonic structures and devices with attractive application potential. Metal thin films, nanowires, and nanoparticles are embedded for achieving surface plasmon resonance (SPR) or localized SPR within PCF structures. This paper begins with an outline of plasmonic sensing principles. This is followed by an overview of fabrication and experimental investigation of plasmonic PCFs. Reported plasmonic PCF designs are categorized based on their target application areas, including optical/biochemical sensors, polarization splitters, and couplers. Finally, design and fabrication considerations, as well as limitations due to the structural features of PCFs, are discussed. © 2017 Optical Society of America

Recent advances in plasmonic photonic crystal fibers: design, fabrication and applications

DORA JUAN JUAN HU AND HO PUI HO

1. INTRODUCTION

Plasmonics, a bridging technology for electronics and photonics, has been extensively studied and widely explored for nanophotonics, magneto-optic data storage, microscopy, solar cells, and sensing applications such as biological and chemical detection [1,2]. Surface plasmon (SP) waves are coupled electron–photon modes at the boundary between a metal and a dielectric. Generally, plasmonic sensing devices are categorized into two types: propagating surface plasmon resonance (SPR) sensors and localized surface plasmon resonance (LSPR) sensors. Because of the momentum mismatch between SPs and photons propagating in vacuum, special configurations are needed to excite the plasmon modes.

Compared with prism coupling in traditional bulk-optic systems, SPR optical fiber offers a more compact and robust configuration with potential in remote and *in situ* monitoring applications. The first SPR optical fiber was proposed and demonstrated in 1993. It showed comparable sensitivity to bulk SPR systems, thus paving a promising path for the development of plasmonic fiber optic technology and applications [3]. Since then, numerous plasmonic fiber optic structures based on simulation and experimental studies have been reported in literature. Various fiber types such as single-mode fibers (SMFs) [4], multimode fibers (MMFs) [5,6], hollow fibers or capillaries [7,8], tapered fibers [9–11], U-shaped fibers [12,13], D-shape fibers [14,15], side-polished fibers [16,17], and fiber tips [18,19] have been demonstrated for enhancing sensor performance. Fiber grating technologies have also been incorporated to further improve sensitivity, and multiple channel sensing capability has been demonstrated through fiber Bragg grating SPR sensors [20,21] and fiber long period grating SPR sensors [22,23].

Photonic crystal fibers (PCFs), also known as microstructured optical fibers, or holey fibers, contain axially aligned air holes that can be arranged periodically or non-periodically in the cladding region centered on a solid or hollow core. These fibers provide unique features and flexibilities not attainable in conventional optical fibers. Since its discovery in 1996, the past two decades have witnessed substantial development of PCF technology for sensing, communication, and medical applications [24,25]. Particularly for sensing applications, PCFs have attracted significant attention in light of the ever-increasing demand for high-performance sensing devices [26]. The incorporation of plasmonic structures into PCFs seems a natural move of plasmonic fiber optic technology, as PCFs allow unparalleled flexible control of waveguiding properties through engineering of holey structures. As a desirable platform for plasmonic structures, PCFs enable and enhance many application opportunities in terms of performance and versatility.

The potential impact of plasmonic PCFs has resulted in growing effort in developing new device features for all kinds of applications. The most recent review article on this topic focuses on PCF-based SPR chemical sensors [27]. Other review articles focus on optical fiber sensors with SPR or LSPR structures in general [28–32]. Therefore, there

exists a need to have a comprehensive review on using PCFs as a platform for both SPR and LSPR structures for a wider spectrum of applications. including temperature sensors and polarization splitters. In this review, we first summarize the current state-of-the-art achievements in the design, fabrication, and application experiments of plasmonic PCFs. We then identify important research directions for the research community. This review begins with an introduction of the operating principles of plasmonic fibers, followed by an overview of the progress in fabrication techniques and experimental studies. In the second half of this review, we present a summary of various plasmonic PCF structures, which are classified based on their respective applications with benchmarking, and a discussion of their opportunities and challenges.

2. OPERATING PRINCIPLE OF SPR FIBERS

Surface plasmon waves (SPWs) are electron oscillations guided by an interface between two materials having negative and positive real parts of permittivity. This type of interface is often implemented with a metal–dielectric layer stack. SPWs can be excited by photons when the parallel optical wave vector matches the propagation constant of the corresponding SPW. In an optimized system, an excited SPW can propagate over a long distance with a significant portion of the optical energy being converted to the guided mode. The basis of SPR, which has been extensively used for sensing applications, indeed arises from this wave vector matching requirement, as the extent of energy transfer from photons to SPWs is very sensitive to a number of parameters, such as refractive index (RI) of the medium adjacent to the metal–dielectric interface. A widely adopted practical realization of the SPR sensor is the Kretschmann configuration [33], in which an inverted metal-coated prism exhibits attenuated total internal reflection when matching of wave vectors takes place at the metal–glass interface. The metal commonly used is gold because of its chemical stability. Silver provides better performance, but is seldom used in practical systems due to its poor chemical stability. In the case of optical fiber SPR sensors, efficient coupling can be achieved by exposing the core either by side-polishing [34] or selective etching in hydrofluoric acid [35]. Figure 1 shows a typical SPR sensor configuration based on the Kretschmann and fiber configurations.

Since the excitation of SPWs can be exactly described by the transfer matrix technique, one can readily use Fresnel's equations [36,37] to represent the ratio between

Figure 1
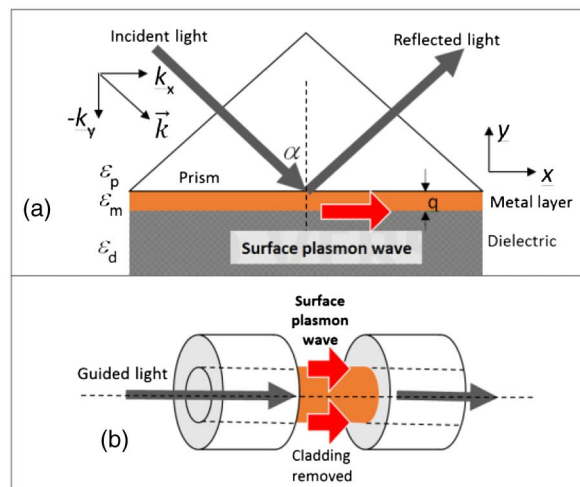
Typical SPR sensor based on the (a) Kretschmann and (b) fiber configurations.

the incident and reflected electric fields in the system. SPR results in significant optical energy dissipation in the *p*-polarized component because of coupling of SPW while leaving the *s*-polarized component unaffected. Equation (1) shows the phase and amplitude of the reflected *p*-polarized component:

$$r_{\mathrm{pmd}} = |r_{\mathrm{pmd}}|e^{j\phi} = \frac{E_r}{E_i} = \frac{r_{pm} + r_{md}\,\exp(2iK_{my}q)}{1 + r_{pm}r_{md}\,\exp(2iK_{my}q)}, \tag{1}$$

where r_{pmd} represents the reflection coefficient of the prism–metal–dielectric structure, $|r_{\mathrm{pmd}}|$ the amplitude, ϕ the phase, E_r and E_i the reflected and incident electric filed, respectively, q the metal thickness, and

$$r_{kl} = \frac{\varepsilon_l k_{ky} - \varepsilon_k k_{ly}}{\varepsilon_l k_{ky} + \varepsilon_k k_{ly}}, \tag{2}$$

$$K_{ky} = \sqrt{\left(\frac{2\pi}{\lambda}\right)^2 \varepsilon_k - K_x^2}. \tag{3}$$

Here, the subscripts x and y correspond to the coordinate system shown in Fig. 1, where k, l are p (prism), m (metal), and d (dielectric), λ is the incident wavelength, K is the propagation constant of the evanescent wave at the prism–metal/metal–dielectric interfaces, and ε_p, ε_m, and ε_d are the permittivities of the prism, metal, and dielectric respectively.

The transfer matrix technique is highly desirable to treat multilayer structures. It is a type of an *ab initio* calculation to get close reproduction of the reflection properties in reality, i.e., a dip in the reflection as described in Eq. (1) corresponds to the resonance of SP excitation.

An intuitive approach is to investigate the dispersion relations of the waves in the waveguides. The propagation constant of the SP along the metal–dielectric interface is matched to the parallel component of the wave vector in the dielectric. The phase-matching conditions in plasmonic fibers are satisfied at the intersections of the effective mode index of the core mode and the SPs. At phase-matching wavelengths, the real part of the effective mode index of the fiber waveguide and the SPs are equal. In addition, the confinement loss of the fiber waveguide mode, which is a function of the imaginary part of the effective mode index, would exhibit a peak at the phase-matching wavelengths corresponding to SP excitation.

In metal nanowire filled fiber structures, surface plasmon-polariton (SPP) modes can be excited and coupled from the fiber core modes. This structure can be viewed as fiber directional couplers, possessing a dielectric waveguide for a core guide mode and a metal wire waveguide for SPP modes. The coupling system generally requires numerical simulation for electromagnetic wave analysis of dispersion relations and loss properties. The metal-wire-filled fibers usually possess strong polarization-dependent properties. Figure 2(a) illustrates an example of a gold-wire-filled silica PCF [38], showing its dispersion relations on the coupling between the core mode of the fiber and a few SPP modes of the gold wire in Fig. 2(b). At phase-matching wavelengths, strong coupling between the core mode and the SPP mode can be observed in Fig. 2(c), corresponding to peaks (SPP mode excitation) in the confinement loss spectrum, as shown in Fig. 2(d).

The SP excitation in thin film coated fibers can be understood from the planar metal–dielectric structure as shown in Fig. 1. The guided light in the fiber core would

generate an evanescent wave at the dielectric–metal interface. The evanescent wave would excite the SPs at resonance wavelengths. An example of metal thin-film-coated fiber structure, the dispersion relation and the loss at the proximity of the SP excitation, and the mode profiles of the fiber waveguide mode and the plasmon mode at the phase-matching condition is presented in Fig. 3 [39].

Different from propagating SPs, metal nanoparticles (NPs) are embedded for achieving LSPR within fiber structures. The excitation of LSPR results in a highly localized electromagnetic field outside the metal NPs. Numerical simulations are usually required for the analysis of the surface field except for simple systems such as spherical NPs with bigger size, which can be treated by analytical calculations, e.g., Mie theory. Unlike SPR structures, LSPR can be directly excited as the illumination frequency matches the eigenfrequency of the LSPR [40]. A gold nanostar array was designed to achieve a wide LSPR band, e.g., 530–620 nm, so that could cover both the excitation wavelength and the emission wavelength of Raman scattering [41]. The gold LSPR array design on a fiber facet and the LSPR field intensity and mode profile are presented in Fig. 4. The LSPR can be tuned by altering the size, shape, and composition of the NPs [41].

Changes of both the amplitude and the phase under resonance conditions are extremely sensitive to variations in the ambient RI n_d (with $n_d = \sqrt{\varepsilon_d}$ if the material is a non-magnetic medium) in the dielectric layer. Because of the dispersive nature of the resonance, spectral response can also be used as a detection parameter. It is the

Figure 2
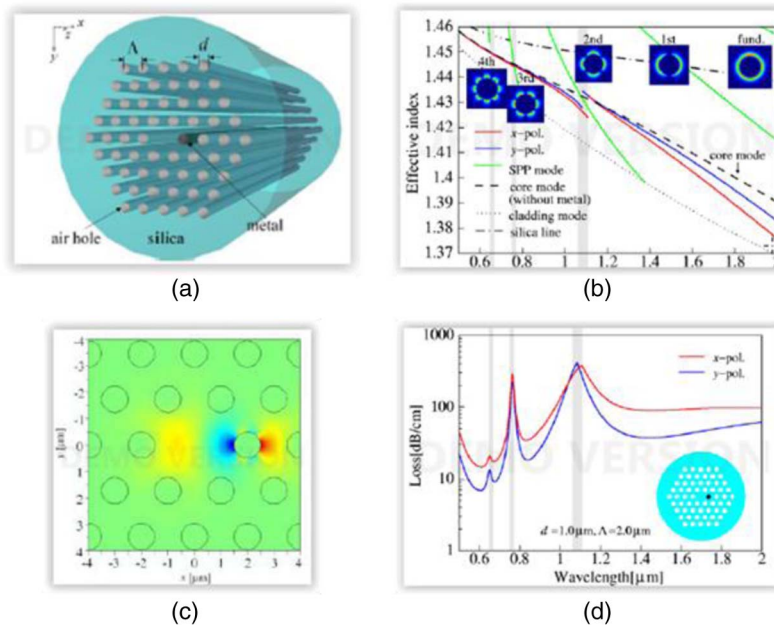
(a) Schematic representation of a PCF with a metal wire. (b) Dispersion relations of metal-wire-filled PCF: x-polarized (red curve) and y-polarized (blue curve) core modes, the SPP modes of different orders excited on the gold wire (green curves), core mode without metal wire (dashed black curve), cladding mode (dotted curve), and index of silica material (dashed–dotted curve). The SPP mode profiles of the gold wires are shown as inset figures. (c) Mode profile of the x-component of the electric field distributions of the x-polarized core mode at a phase-matching wavelength. (d) Confinement loss of the x-polarized (red curve) and y-polarized (blue curve) core modes. Reprinted with permission from [38]. Copyright 2011 Optical Society of America.

shifts in amplitude, phase, and spectral characteristics that constitute the basis of SPR sensors, which is well known for their high performance in detecting small changes of RI on the metal surface caused by conjugation of biomolecular species. This technique has a major advantage over its fluorescence counterparts because of the "label-free" measurement approach. Users may use their samples without having to treat them with fluorescence tags. Moreover, there is no issue associated with photobleaching.

3. REVIEW OF THE FABRICATION PROCESS AND EXPERIMENTAL STUDIES OF PLASMONIC PCF STRUCTURES

3.1. Metal-Nano/Microwire-Filled Plasmonic PCF Structures

Plasmonic nanowires, such as those made from gold and silver, are the constituents widely used for creating nanoscale metallic structures in plasmonic waveguides. In a plasmonic fiber structure, guided SPPs can be excited and supported in metallic nanowires when fiber core guided modes are phase matched to the SPP modes, thus resulting in distinct resonances of fiber core guided modes. The fabrication of metallic nanowires in a PCF can be done during [42,43] or after [44–47] the PCF drawing process.

The drawing approach was achieved through incorporating the Taylor-wire process [48] into the stack-and-draw procedure for silica PCFs and polymethyl methacrylate (PMMA) fibers [42,43]. First, six silica-coated copper rods were stacked together with 114 hollow capillaries around a single solid silica rod to form the structure of interest. The stack was inserted into another silica tube for high-temperature drawing. Scanning electron microscopy (SEM) images of the fabricated PCF with six copper wires are shown in Fig. 5. The copper wire diameter was around 4 μm [42]. Tuniz *et al.* demonstrated a co-drawing of PMMA PCFs with PMMA and indium, and

Figure 3
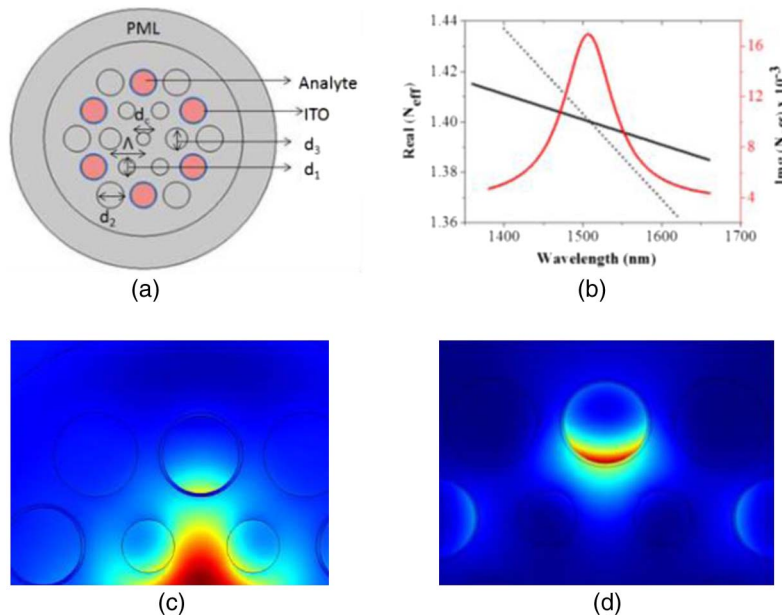
(a) Cross section of the proposed sensor. (b) Dispersion relations of core guided mode (black solid line), plasmonic mode (black dotted line) and imaginary part of core guided mode (solid red). (c) Plasmonic excitation of core guided mode and (d) plasmon mode. © 2014 IEEE. Reprinted with permission from Dash and Jha, IEEE Photon. Technol. Lett. **26**, 594–598 (2014) [39].

experimentally showed that the polarization-dependent transmission property of the fiber was useful for terahertz filtering and polarizer applications [43]. The fiber drawing method was also shown to be useful for the fabrication of metallic nanowires and microwire arrays [49,50]. Apart from the Taylor-wire process, a gold-filled cane was used to fabricate high-quality gold wires of diameter down to 260 nm and length of more than 100 m in standard step index fibers through direct drawing [51]. This method permits more precise control over fabrication parameters, e.g., location of the gold wire in the fiber [51].

The high-pressure microfluidic chemical deposition technique was employed to fabricate silicon tube and germanium-wire-filled PCFs [44]. In this approach, high pressure was used to generate mass transport of gas phase precursors through the length of fiber.

Two other fabrication methods for filling the hollow channels with metals and making metallic nanowires within the PCF channel without the need of organic precursors have been reported. Namely, the techniques are based on a high-temperature pressure cell [45,46] and pressure-assisted splicing [47]. The first was introduced for producing high-purity metal nanowire arrays within PCFs, through pumping molten metal from a high-temperature (around 1100°C) pressure cell into hollow channels of PCFs under high pressure up to 60 bars. The smallest nanowire diameter realized in the experiment was 550 nm. Up to 40 mm penetration lengths of the nanowires were achieved with excellent optical quality. SEM images of the end face of a gold-filled PCF is shown in Fig. 6. The PCF structure has been well preserved because the melting temperatures of the metals, e.g., gold and silver, are well below the softening temperature of silica [45].

Figure 4

(a)   (b)

(c)
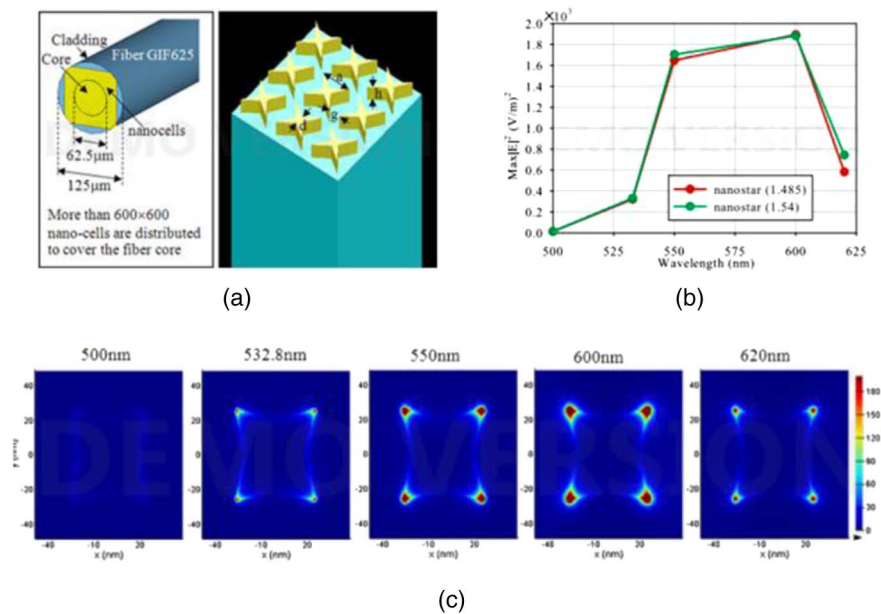
(a) Gold nanostars on a fiber facet with an illustration of 3×3 unit cells: the image plane is at 1 nm above the top of the nanostar surface; $a = 52$ nm, $g = 45$ nm, $h = 40$ nm, and $d = 20$ nm for the 633 nm design and $d = 40$ nm for the 533 nm design. (b) Max$|E|^2$ of the 533 nm nanostar at the image plane with incident electric field of 1 V/m. (c) $|E|^2$ of the 533 nm nanostar at the image plane with a color bar maximum of 200 $(\text{V/m})^2$. Reprinted with permission from Sun *et al.*, Appl. Phys. A **115,** 87-91 (2014) (Figs. 1, 3, and 5) [41]. Copyright 2013 Springer-Verlag Berlin Heidelberg.

The high-temperature pressure cell technique was used for selective infiltration of individual air holes with gold nanowires by postprocessing the PCF structure before pumping in the molten metal. The postprocessing technique was based on inflating a PCF heated on a tapering rig, and pressurizing the holes from one end while the other end is sealed [52]. A polarization-maintaining PCF was selectively blocked using the postprocessing technique and subsequently infiltrated with gold nanowires using the pressure cell technique at pressures up to 190 bars, with a 900 nm diameter gold wire length up to 20 mm. Because of SPR coupling, highly polarization- and wavelength-dependent transmission was observed [46].

The second technique was based on splicing a PCF to a filling capillary having outer and inner diameters of 200 and 80 μm containing a metallic wire, typically at a diameter of 50 μm [47]. The metal wire was manually inserted into the capillary and pushed farther into the capillary, leaving an empty section for splicing. The end portion of the capillary was cleaved and spliced to a silica PCF using a Vytran splicing machine. Argon gas at a pressure of several hundred bars was applied to push the molten metal into the hollow channels. This method is suitable for non-wetting materials, for example, gold, silver, gallium, germanium, and chalcogenide glasses, which have melting temperatures significantly lower than the softening temperature of silica. Selective infiltration of metallic wire can be realized by using an intermediate capillary as a mask between the filling capillary and the PCF. Wires with diameters as small as 120 nm were realized in the experiment. The aforementioned methods were reported to fabricate metal nano/microwires with diameters ranging between 120 and 4 μm and length up to 20 cm, as a permanent part of the fiber to form desirable plasmonic PCF structures [47]. This technique has successfully produced a fully filled solid-core

Figure 5
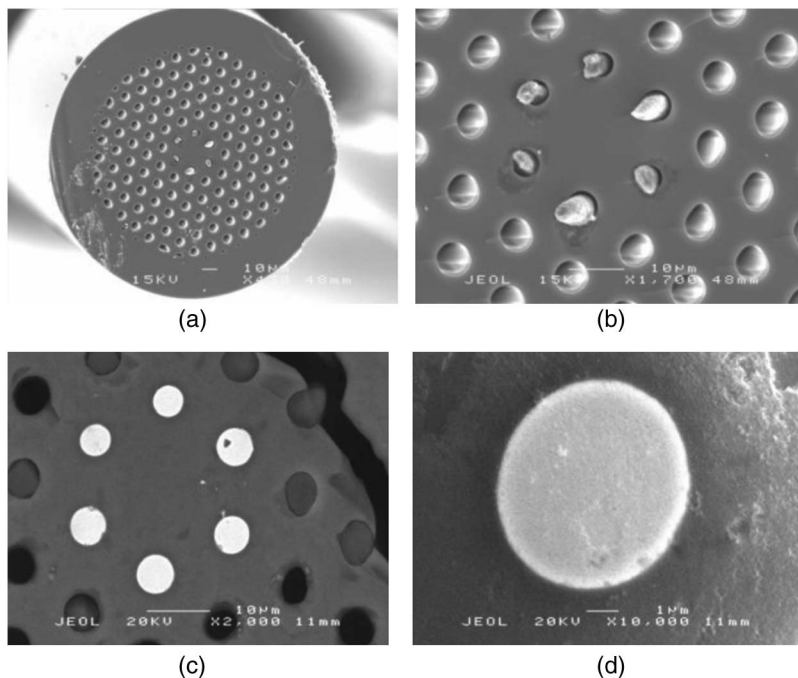
SEM images of metallic optical fiber with one ring of copper rods. (a) shows a cleaved fiber end face with six copper wires protruding from the surface. (b) Higher magnification image of the six copper wires. (c) Backscattered electron image of the polished fiber sample end face. (d) Shows details of the copper rods in (c). Reprinted with permission from [42]. Copyright 2008 Optical Society of America.

photonic crystal fiber (SCPCF), a selectively filled PCF, and a modified step index fiber with a parallel gold nanowire, as shown in Fig. 7 [47]. A transmission measurement setup consisting of a supercontinuum source and an optical spectrum analyzer was used to characterize the transmission characteristics of the as-fabricated gold-wire-filled PCF. By using a polarizer and a half-wave plate between the light source and the fiber, the input polarization was precisely controlled. The intensity distribution of the SPPs and the polarization characteristics in a PCF with a gold nanowire array were measured using scanning near-field optical microscopy [53]. A single-wire-filled and a double-wire-filled PCF were measured and showed polarization-dependent attenuation spectra. Polarization splitting was observed for the double-wire-filled PCF [54].

More recently, Jain *et al.* reported fabrication of micrometer-sized gold nickel alloy wire in a graded index silica fiber by the pressure assisted melt filling technique to address the mechanical and chemical weakness of pure metals [55]. The fiber contained a germanium-oxide-doped graded core and an empty channel parallel to the core, which was filled with the gold nickel alloy using pressure assisted melt filling technique.

Instead of fabricating a metal nanowire structure within a PCF, Lu *et al.* reported preparation of silver nanowire solutions in ethanol and chloroform for infiltration in PCFs for temperature sensing measurements [56,57]. In this approach, the authors used capillary effects in the air holes to drive the liquid into the channels, with a penetration depth up to several centimeters. In the experiment, the silver nanowire colloid was a stable translucent colloidal suspension of silver nanowires in ethanol carrier. The liquid was a physical mixture of ethanol and chloroform. The diameter of the nanowires was about 90 nm, and the average length was about 30 μm. The mixing volume ratio of the silver nanowire solution and the chloroform was changed to tune the plasmonic resonance and the transmission loss.

The characteristics of the metal wires in different PCFs structures are summarized in Table 1. Depending on different fabrication conditions, e.g., temperature, pressure,

Figure 6
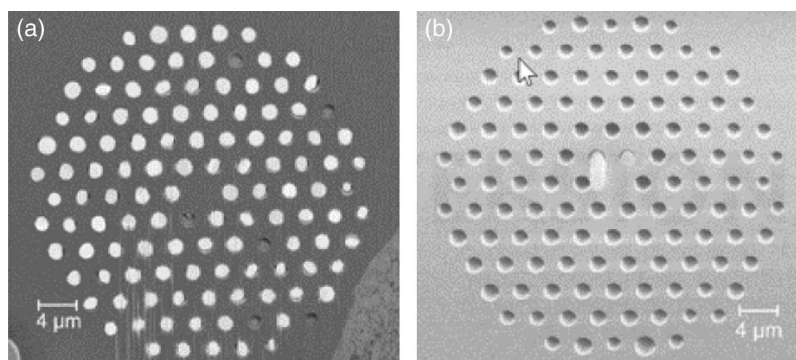
(a) SEM of the end face of a cleaved metal-filled PCF, polished by focused ion beam etching (hole diameter of 1.52 μm, hole spacing of 2.9 μm). The wires undergo ductile thinning during cleaving, breaking at random positions. Those that protrude from the end face are polished and appear as bright disks in the SEM; the rest (six in total) are dull in appearance. (b) SEM image of the unpolished end face of a PCF with two metal nanowires located next to the solid core. Reprinted with permission from Schmidt *et al.*, Phys. Rev. B **77**, 033417 (2008) (Fig. 1) [45]. Copyright 2008 by the American Physical Society, https://doi.org/10.1103/PhysRevB.77.033417.

and usage of precursor, metal-wire-filled PCFs have been reported mainly on silica and PMMA PCFs, and various metal materials, showing different outcomes of the metal wire characteristics, e.g., diameter and length.

3.2. Metal-Coated Plasmonic PCF Structures

Successful deposition of metallic layers and/or semiconductors inside PCF structures with high precision is a major step toward the realization of all-fiber optoelectronics. Indeed, the chemical vapor deposition (CVD) approach is a well-established technique for conducting highly controlled deposition of semiconductors and metals from chemical precursors. Sazio *et al.* reported high-quality conformal deposition of semiconductor and metal within the voids of PCFs through high-pressure microfluidic chemical deposition [58]. The air holes of PCFs acted as micro/nanoscale CVD reaction chambers. Very high pressure levels ranging from 10 to 100 MPa were used to facilitate rapid mass transport inside the fiber pores. Figure 8(a) shows the formation of a 80-nm-thick smooth annular gold layer on top of another CVD-deposited silicon tube, thus leading to the formation of a Schottky junction, inside a PCF by means of sequential deposition. One can individually address the holes to produce customized material films on each capillary wall, thus opening the possibility to form patterned plasmonic PCFs. Figure 8(b) shows an array of gold particles written with a 1.6 µm capillary.

Boehm *et al.* reported an optimized chemical coating method based on the silver mirror reaction (also known as the Tollens reaction) for silver deposition on the internal

Figure 7
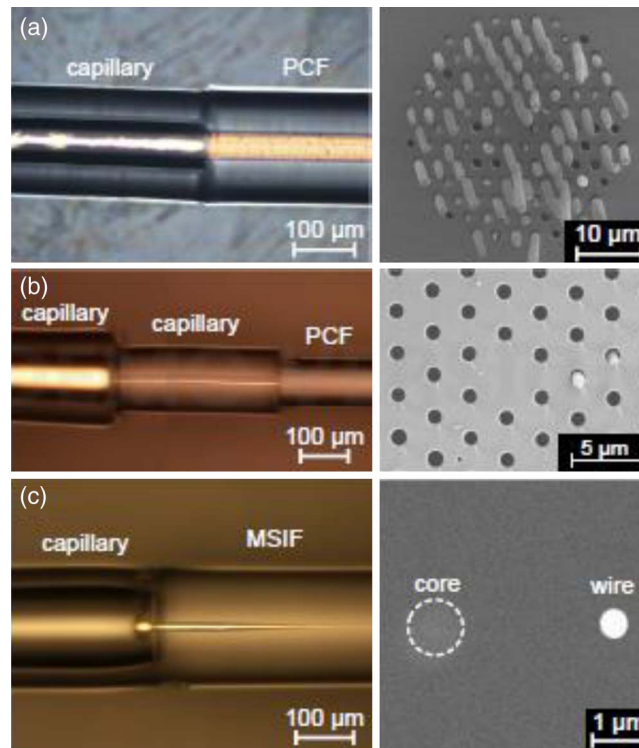
Optical side-views of the splices (left-hand column) and SEM images of the cleaved end faces (right-hand column). (a) Solid-core PCF with all its channels filled with gold. (b) PCF in which only two channels are filled with gold. (c) Modified step index fiber with a parallel gold nanowire. Reprinted with permission from [47]. Copyright 2011 Optical Society of America.

Table 1. Characteristics of the Metal-Wire-Filled PCFs

Fabrication Technique	Wire Diameter (μm)	Wire Length (mm)	Fabrication Condition	Features and Properties[a]	Reference
Modified stack-and-draw technique (combination of Taylor-wire process)	4.2	70	High temperature, e.g., 1880°C	Silica PCF with single or a few copper microwires; the attenuation was measured.	Hou 2008 [42]
Modified stack-and-draw technique (combination of Taylor-wire process)	<10	Up to kilometer	Low temperature, e.g., 156.6°C	PMMA fiber with indium wire array; transmittance was measured via terahertz time domain spectroscopy.	Tuniz 2010 [43]
Pressure-assisted melt filling technique	1.3	Up to 8.1	High temperature, e.g., 1100°C; high pressure, e.g., 50 bar	Silica fiber with AuNi micrometer sized wire array; the attenuation was measured by the cut-back technique.	Jain 2016 [55]
High-pressure microfluidic chemical deposition technique	5	Several centimeters	High temperature at 700°C, high pressure, organic precursor, e.g., GeH_4 germane precursor at 2 MPa partial pressure in Ar was flowing at a total pressure of 40 MPa	Silica PCF with silicone and germanium microwires; the deposited material was studied by Raman spectroscopy, and electrical characterization was conducted on resistivity and carrier type, mobility, and concentration.	Finlayson 2007 [44]
High temperature pressure cell technique	0.55	Up to 40		Silica PCF with single and multiple sub-micrometer Au or Ag wires; the SPR excitation and coupling from the fiber core mode was characterized by transmission spectrum measurement.	Schmidt 2008 [45]
	0.9	24.5	High temperature, e.g., 1100°C; high pressure, e.g., 60 bar	Silica PCF with single sub-micrometer Au wires; due to SPR coupling, highly polarization- and-wavelength-dependent transmission was observed.	Lee 2008 [46]
Pressure-assisted splicing technique	0.12–4	Up to 200	Filling pressure of 300 bar	Silica PCF with multiple sub-micrometer and micrometer Au wires; optical transmission spectra were measured and showed dips at wavelengths where guided surface plasmon modes on the nanowire phase match to the glass core mode.	Lee 2011 [47]
				Intensity distribution of the SPPs and the polarization characteristics in a PCF with a gold nanowire array were measured using scanning near-field optical microscopy.	Uebel 2012 [53]
				A single wire-filled and a double wire-filled PCF were measured and showed polarization-dependent attenuation spectra; polarization splitting was observed for the double wire-filled PCF.	Lee 2012 [54]
Combined method of fiber drawing with advanced filling materials	0.05	1.5 m	High temperature at 850°C	Zinc microwires embedded in glass matrices; the microwires were analyzed by taking SEM and energy-dispersive x-ray spectroscopy.	Zhang 2008 [49]
Iterative co-drawing of multimaterial in polymer matrices	0.015	Few hundred meters	Low temperature <240°C	Semiconducting and piezoelectric nanowire and nanotube arrays in a polymer matrix; the electrical and photo conductivity were measured	Yaman 2011 [50]
Capillary effect infiltration technique	0.09	0.03	Infiltrated in room temperature	Ag nanowires mixed in solution. The SPR induced resonance was measured for sensing applications.	Lu [56,57]

[a]Unless mentioned, the plasmonic effects in the fibers were not studied in the work.

surfaces of PCFs. The Tollens reaction was optimized to coat a 60-nm-thick silver layer over a 1-m-length suspended core fiber with three large holes around the solid core [59].

A two-stage draw process was used in the fabrication of microstructured polymer optical fiber (mPOF). A selective silver coating was realized by suction and evaporation of metal nanoparticle mixtures into the desirable holes in the fiber preform with other holes plugged with glue. The reaction mixture was an aqueous solution of dextrose and silver nitrate. Zhang *et al.* used this technique to demonstrate selective silver coating in an mPOF up to 40 cm of penetration into the length of the fiber. However, the coating was rough and granular, as shown in Fig. 9 [60].

Instead of depositing high-quality metal films inside the holes of PCFs, some groups proposed to deposit a metallic coating outside the fiber. The primary challenge is to produce efficient excitation of SPs from the guided mode, which can be achieved by bringing the metallic coating closer to the fiber modes for efficient coupling. One possible structure is an exposed core holey fiber, which is a modified suspended core fiber where one side of the core is exposed axially. Klantsataya *et al.* reported an experimental demonstration of fabricating thin silver film on the exposed core of the PCF using an electroless plating method involving a pre-treatment step and an electroless plating process [61]. The fiber samples were thoroughly cleaned and sensitized, and subsequently treated with precipitation of metallic silver from ammoniacal silver nitrate solution in the presence of a reducing agent. An SEM image of the exposed core PCF and the plasmonic PCF structure with silver thin film depositions are shown in Fig. 10. Approximately 50-nm-thick silver thin film was deposited on a 1-cm-long mPOF. This deposition technique can be used for multiple sensor fabrication up to 10–15 samples. The plasmonic fiber was enclosed in a flow cell for liquid measurement, showing RI sensitivity of 1800 nm/RIU [61]. A similar structure of side hole polymer PCF was reported for SPR sensing, comprising holey cladding, and a

Figure 8
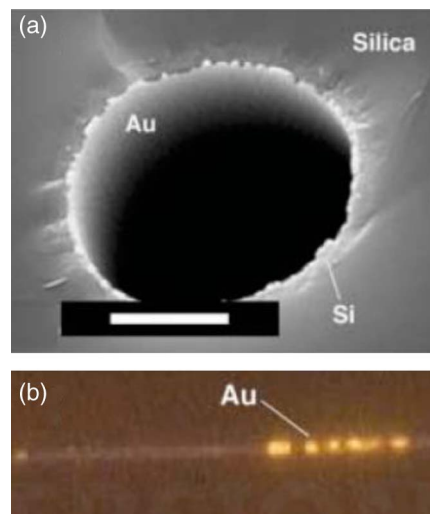
(a) An 80 nm thick smooth gold annulus deposited on a silicon tube. Contrast between silica and silicon is low. Scale bar, 2 mm. (b) Optical micrograph of an array of gold particles written with a focused 514.5 nm laser beam within a 1.6 mm capillary. From Sazio *et al.*, *Science***311**, 1583–1586 (2006) [58]. Reprinted with permission from AAAS.

side hole to expose the core so that direct sputtering of gold was able to deposit the desired metal layer on the core surface [62].

Partial cladding can be etched or side polished from the fiber to enhance an evanescent field for SP excitation. A PCF was side polished by 57 µm, and the polished surface was subsequently sputtered with gold to form a thin layer around 34–35 nm in thickness [63]. The fabricated plasmonic PCF structure was then tested for fluorescence spectroscopy detection of Rhodamine B (RhB) with concentration from 10 to 100 µM using the SP effect.

Partial or complete collapsing of holey cladding enables excitation of higher order modes to reach the outer surface of the PCF. This technique is popular for producing

Figure 9
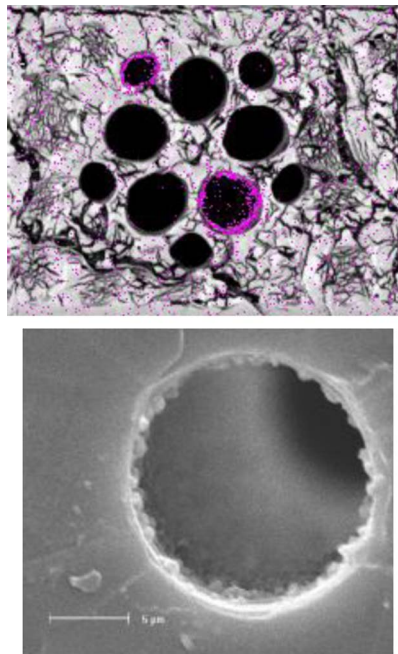
Low magnification SEM micrograph of plasmonic mPOF, showing two coated holes (top). Elemental analysis shows the presence of silver (dots in the image). SEM image of the silver surface of a coated hole is shown on the bottom. Reprinted with permission from [60]. Copyright 2007 Optical Society of America.

Figure 10
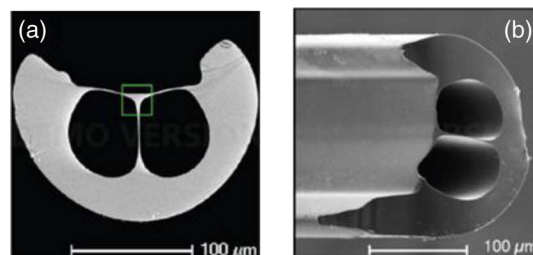
(a) Exposed core fiber (ECF) cross section with a triangular core and (b) silver film deposited on ECF. Reproduced from [61] under the terms of the Creative Commons Attribution 4.0 License. http://creativecommons.org/licenses/by/4.0/.

PCF interferometers for liquid detection and biosensing [64,65]. Wong *et al.* employed this technique in developing a plasmonic PCF biosensor [66]. The PCF sample was spliced between two multimode fibers, with a fully collapsed zone over length of 126 µm. The fiber was then cleaned, dried, and fixed onto a platform for sputtering gold coating around its surface. The gold-coated PCF was subsequently chemically treated to form a thiol and protein G coating on the gold surface, and was used to measure the binding kinetics of the IgG (anti-IgG) complexes with a minimum detection limit at concentration of 0.267 mg/L of anti-IgG.

Tapered PCFs with subwavelength cores can provide a substantially enhanced evanescent field. A metalized nanostructured PCF taper with gold film perforated on the cross section of the taper by using the thermal evaporation technique was reported to show enhanced transmission peaks in the spectral domain [67]. The characteristics of the metal coatings in different PCF structures are summarized in Table 2.

3.3. Plasmonic PCF Structures with NPs

NPs have been extensively studied for applications involving LSPR, in particular surface-enhanced Raman scattering (SERS) due to its unique molecular specificity. The combination of plasmonic NPs and PCFs offers the unique benefit of working with extremely low sample volume and long interaction length. Clearly there exist captivating advantages and promises for developing fully integrated plasmonic devices especially for sensing applications.

The most straightforward method for NP deposition on the inner surface of PCFs is to infiltrate the NP solution into the air holes by the capillary effect. After a heating and drying process, the NPs are attached to the inner surface by the opposite charge affinity [68]. The PCF is subsequently filled with the analyte solution. Fiber structures with immobilized NPs are categorized as coated PCFs thereafter. Using this method, Yan *et al.* reported a SCPCF with four large air holes surrounding the solid core and surface coated with gold NPs for SERS detection [69]. The NPs can be mixed with the analyte solution and filled into the air channels of PCFs, which does not require a drying process. Structures fabricated with this technique are categorized as liquid filled SCPCFs. Xie *et al.* reported a silver-NP-filled SCPCF SERS probe for detection of the 4-Mercaptobenzoic acid solution [70]. Zhang *et al.* demonstrated an ultra-low SERS detection limit of 50 fM by using an optimized SCPCF structure filled with gold NPs and Rhodamine 6G (R6G) solution [71].

Hollow-core photonic crystal fibers (HCPCFs) were introduced in the design of SERS detector probes at the same time in order to address a few challenges faced by SCPCFs, which include weak evanescent fields in the voids for improved Raman signal excitation and suppression of the strong Raman background signal from silica [72–74]. HCPCFs with NPs immobilized on the inner surface of air holes through the infiltration and drying procedures are categorized as coated HCPCFs. Liquid-filled HCPCFs refer to structures that are completely filled with a physical mixture of NPs and analyte. The geometry of silver NPs was optimized for enhanced SERS detection in a liquid-filled HCPCF [75]. Improvements of SERS performance were made by sealing/collapsing the air holes in the cladding and infiltrating the hollow core with a mixed solution of NPs and analyte for forming a liquid core photonic crystal fiber (LCPCF) [76–78]. The enhancement was attributed to increased SERS active volume as a result of good confinement of both light and analyte in the central core. Higher sensitivity was later demonstrated using an inner-wall-coated LCPCF probe with a sandwich structure, i.e., two types of silver NPs were used as SERS substrates simultaneously. The hollow core was selectively coated with NPs first and selectively filled with a mixed solution of NPs and the analyte [79]. Only the central core was

Table 2. Characteristics of the Metal-Coated PCFs

Fabrication Technique	Coating Thickness (nm)	Coating Length (mm)	Fabrication Condition	Features and Properties[a]	References
High pressure microfluidic chemical deposition	25	70	High pressure, e.g., 10–100 MPa; organic precursor, e.g., GeH_4, SiH_4; high temperature, e.g., 700°C	Conformal coating of germanium, silicon in silica PCF; transconductance measurements were carried out to characterize the performance of the semiconductor structure fabricated in the PCF.	Sazio 2006 [58]
Chemical deposition by Tollens reaction	60	1 m	Room temperature, medium pressure, e.g., 100 psi	Suspended core fiber with silver coating; the angular position of SPR features were measured for a slide with chemically deposited silver and a slide coated using sputtering; the fiber was not measured for SPR signal.	Boehm 2011 [59]
Two-step fiber drawing method	Granular coating	40 cm	Low temperature, e.g., for polymer fiber drawing	Polymer PCF with selective silver coating. The polarization-dependent transmission of the silver coated fiber was experimentally measured.	Zhang 2007 [60]
Chemical plating technique	50	10	Precipitation of metallic silver from ammoniacal silver nitrate solution	Exposed core silica fiber with silver coating; performance of the sensor in terms of its RI sensitivity and FWHM of SPR response were experimentally investigated.	Klantsataya 2015 [61]
Sputtering technique	37	6	Ar-ion physical sputtering	Polymer side hole PCF with gold coating; SPR features were experimentally measured for fluid sensing.	Wang 2009 [62]
	34–35	10.5		D-shaped silica PCF with gold coating; the SPR field enhancement of the fiber sensor was experimentally demonstrated with an improvement in fluorescence emission intensity and higher sensitivity in fluorescence spectroscopy.	Yu 2011 [63]
	30, 50, 60	5–20		Gold externally coated PCF; the structure was experimentally demonstrated as a SPR biosensor to monitor the binding kinetics of the IgG (anti-IgG) complexes.	Wong 2013 [66]
Thermal evaporation technique	15–200	—	Vacuum	Gold coated on the cleaved end of a tapered PCF; a white light was coupled into the PCF side to produce an enhanced optical transmission in the spectral domain through the plasmonic structure at the tapered end.	Arabi 2011 [67]

[a]Unless mentioned, the plasmonic effects in the fibers were not studied in the work.

filled/coated with NPs in LCPCFs. A more detailed review of HCPCF-based SERS probes can be found in [80].

The infiltration process can also be assisted with a differential pressure, which was reported by Du's group in the development of a forward-propagating full-length SERS-active SCPCF platform with immobilized and discrete silver NPs [81,82]. By adjusting the launching condition, an improved SERS signal was demonstrated in a SCPCF coated with gold NPs [83]. Khetani *et al.* reported a differential pressure system for repetitive characterization of a HCPCF Raman probe and experimentally determined HCPCF filling time is inversely proportional to the pressure difference across the HCPCF in the range of 15–60 psi [84].

A dynamic low-pressure chemical deposition technique for NP layer deposition was reported by Csaki *et al.* and Schröder *et al.*, who used a combination of the self-assemble monolayer technique and microfluidics [85,86]. The inner walls of PCFs were chemically modified by the perfusion of silanes, acting as a chemical adhesive layer for metal NPs due to amino modification. The NP solutions were then incubated by continuous flow. The coating uniformity, e.g., the NP density and the layer thickness, was constant up to 6 m. Figure 11 shows the homogeneous coating density on the local curvature of the capillary-channel cross section and NP monolayer at saturation coverage [85].

The high-pressure chemical deposition technique was reported by Amezcua-Correa *et al.*, employing an organic solvent under high pressure to deliver a silver precursor complex into the fiber holes, followed by a simple thermal reduction of the precursor to form an annular deposition of silver NPs inside the holes. Figure 12 shows the SEM images of silver coating layers achieved by different experimental parameters [87]. The PCFs were typically NP-coated over 15 cm with the central 5–6 cm having the most uniform filling. Their work highlighted the importance of an optimized PCF structure with high numerical aperture for efficient collection and detection of Raman response, low-loss core guided modes with large optical component

Figure 11
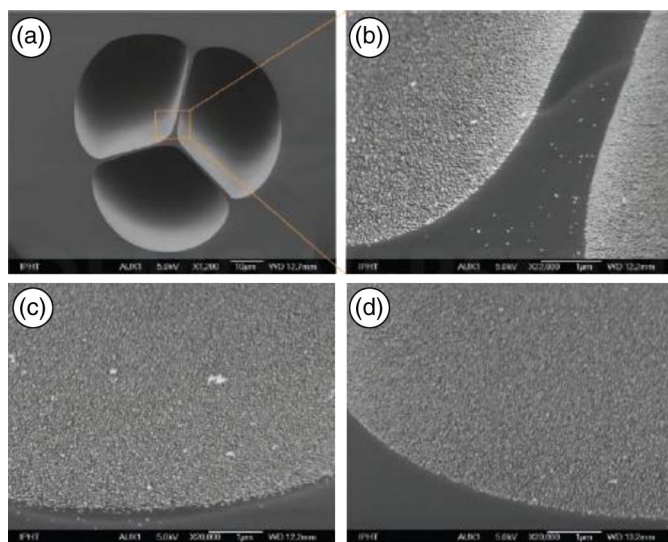
SEM images of the inner walls coated with gold NPs: (a) an overview and (b) zoomed in. (c) Tilted front view of one hole's cross section at the starting point. (d) A view of the fiber end. Csaki *et al.*, Small **6**, 2584–2589 (2010)[85]. Copyright Wiley-VCH Verlag GmbH & Co. KGaA. Reproduced with permission.

propagating in the voids for large excitation area, and long interaction length for improved SERS sensitivity. Optimized fiber structures with increased field–particle overlap were investigated for SERS enhancement by Peacock *et al.* [88].

Using the stack-and-draw technique, Bigot *et al.* fabricated a PCF doped with gold NPs by combining a gold-NP-doped silica core rod with capillaries drawing from silica tubes [89]. A solgel route was used to synthesize a cylindrical rod with interconnected nanometric pores, which was subsequently doped with gold NPs. The gold-NP-doped core rod was surrounded by silica capillaries to form a preform and drawn into a plasmonic fiber.

The integration of the NP-based SERS substrates in a PCF platform has resulted in many successful demonstrations of sensitive, rapid, and compact biosensors for bacterial detection, e.g., *S. oneidensis* [30] and various cancer biomarker detection, including epidermal growth factor receptors (EGFRs) [90], serological liver cancer biomarkers [91], leukemia cells [92], and sialic acid [93]. Core-shell nanotag enabled PCFs have been developed for measuring Raman intensity of rhodamine 6G [94].

The performance figures of the demonstrated NP-based plasmonic PCF devices are summarized in Table 3. The PCFs possess a triangular lattice cladding unless otherwise stated in the table.

4. REVIEW OF PLASMONIC PCF DESIGNS FOR VARIOUS APPLICATIONS

Various designs of plasmonic PCF structures have been proposed to achieve desirable characteristics, e.g., sensitivity, detection range, stability, and miniaturization, for a

Figure 12
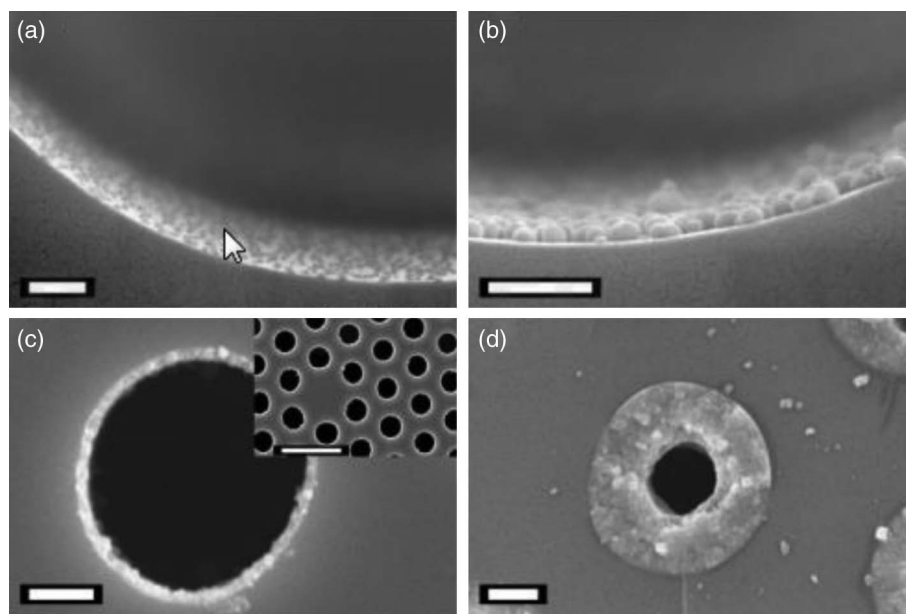
SEM images showing a range of silver deposition profiles obtained by tuning the experimental parameters. A, deposition time = 0.5 h with a precursor concentration of 5 mg mL^{-1}; 1 μm scale bar. B, deposition time = 0.5 h with a precursor concentration of 10 mg mL^{-1}; scale bar is 1 μm. C, deposition time = 2 h with a precursor concentration of 10 mg mL^{-1}; scale bars are 2 and 20 μm on the inset. D, deposition time = 3 h with a precursor concentration of 15 mg mL^{-1}; 2 μm scale bar. Amezcua-Correa *et al.*, Adv. Funct. Mater. **17**, 2024–2030 (2007) [87]. Copyright Wiley-VCH Verlag GmbH & Co. KGaA. Reproduced with permission.

Table 3. Performance Figures of NP-Based Plasmonic PCF Sensors

PCF Characteristics	NPs	Measurand and Techniques	Sensitivity	References
Coated suspended core fiber (SCF) with three large holes	Au	RI based on resonance shift	78 nm/RIU	Csaki 2010 [85]
Coated SCF with three large holes	Au[a]	RI based on resonance shift	80 nm/RIU	Schröder 2012 [86]
		Crystal violet based on SERS	100 μM	
Coated HCPCF	Au	Rhodamine B (RhB) based on SERS	10^{-5} M	Yan 2006 [72]
Coated SCPCF with four large holes in a triangular lattice cladding	Au	RhB based on SERS	10^{-7} M	Yan 2008 [69]
Coated SCPCF	Au	RhB based on SERS	10^{-7} M	Zhang 2013 [83]
Liquid-filled HCPCF with a Kagome lattice cladding	Ag	R6G based on SERS	2.1×10^{-7} M	Cox 2007 [73]
LCPCF	Ag	R6G based on SERS human insulin based on SERS tryptophan based on SERS	10^{-4}–10^{-5} M	Zhang 2007 [76]
Inner-wall-coated-LCPCF	Ag	R6G based on SERS	10^{-6} M	Shi 2008 [79]
Coated SCPCF	Ag	R6G based on SERS	2×10^{-6} M	Oo 2009 [82]
Coated SCPCF	Ag	R6G based on SERS	10^{-7} M	Han 2010 [74]
Coated HCPCF				
Coated SCPCF	Ag	R6G based on SERS	10^{-6} M	Oo 2010 [81]
Coated steering-wheel PCF with three large holes			10^{-6} M	
Coated SCF with three large holes			10^{-10} M	
Liquid-filled HCPCF	Ag	R6G based on SERS	10^{-7} M	Yang 2010 [78]
LCPCF			10^{-10} M	
Liquid-filled HCPCF	Ag	R6G based on SERS	10^{-3} M	Tiwari 2014 [75]
Coated SCF with three large holes	Ag–Au core–shell	R6G based on SERS	10^{-7} M	Pinkhasova 2015 [94]
Liquid-filled SCPCF with a side channel in a triangular lattice cladding	Gold	R6G based on SERS	5×10^{-14} M	Zhang 2016 [71]
Coated SCPCF	Ag	Benzenethiol based on SERS	1 mM	Amezcua-Correa 2007 [87]
LCPCF	ZnO	Polyacrylic acid (PAA) based on Raman spectroscopy	1 mM	Irizar 2008 [77]
Coated SCPCF	Ag	4-aminothiophenol (4-ATP)	0.5 mM	Peacock 2008 [88]
Liquid-filled SCPCF	Ag	4-Mercaptobenzoic acid based on SERS	10^{-6} M	Xie 2009 [70]
LCPCF	Ag	*S. oneidensis* MR-1 strain (bacterial) based on SERS	106 cells/mL	Yang 2011 [30]
Doped SCPCF	Au	Absorption coefficient based on direct measurement of optical attenuation	0.84×10^{-12} cm/W	Bigot 2011 [89]
Protein coated HCPCF[b]	AuNP core SERS nanotag[c]	Epidermal growth factor receptors (EGFRs) based on SERS	10 μg/mL	Dinish 2012 [90]
Protein-coated HCPCF	Au NP core SERS nanotag	Serological cancer biomarkers based on SERS	200 μg/mL	Dinish 2014 [91]
Liquid-filled HCPCF	Ag	Leukemia cells based on SERS	300 cells/mL	Khetani 2015 [92]
Liquid-filled SCPCF with a side channel in a triangular lattice cladding	Au	Sialic acid based on SERS	2 fM	Gong 2015 [93]

[a]The fibers were coated with different types of NPs, e.g., Au, Ag. The Au NP-coated SCF was tested for sensor measurement.

[b]The inner wall of the air holes was coated with protein (analyte) first, followed by infiltration of SERS nanotag solutions.

[c]The SERS nanotag was constructed by absorbing malachite green isothiocyanate (MGITC) molecule onto the gold NPs followed by bioconjugation.

wide range of applications including measurement of RI, dual- or multi-analyte sensing, temperature sensing, dual parameter sensing, biosensing, polarization devices, and couplers. In this section, the plasmonic PCF designs are categorized and reviewed based on their target applications. Gold and silver are two commonly used metals for SPR sensors. Gold- or silver-coated SPR sensors are investigated in visible wavelengths where the plasma frequencies of both materials are located. Specifically, gold is favored because of its availability, chemical stability, and strong SPR signal, which results in good detection sensitivity. On the other hand, silver has a sharp resonance peak, which offers better performance in terms of detection sensitivity.

4.1. RI Sensing and Biosensing

The phase-matching condition of the plasmonic and fiber modes is ultrasensitive to RI. This property has generated immense interest in the exploration of plasmonic fiber designs for RI sensing applications. High RI sensitivity is a key enabler to developing biosensing devices. In 2014, a review paper overviewed PCF-based SPR chemical sensor designs categorized by three types of metallic structures and various PCF structures [27]. In this section, the pioneering and key designs are emphasized and designs reported from 2014 and onward are presented. The key designs were selected based on the authors' perspectives with the best effort to represent plasmonic PCF designs of the same class.

Phase-matching conditions in plasmonic fiber sensors are assessed at the intersections of the effective mode index of the core mode and the SPs, i.e., at phase-matching wavelength, the real part of the effective mode index of the fiber waveguide and the SPs are equal. An important parameter, i.e., the confinement loss, which is related to the imaginary part of the effective mode index of the fiber waveguide mode, is usually used for characterization of the plasmonic sensor, especially for amplitude interrogation and wavelength interrogation methods.

The confinement loss of the waveguide core modes can be obtained from

$$\alpha = 8.686 \times \frac{2\pi}{\lambda} \text{Im}(n_{\text{eff}}) \times 10^4, \tag{4}$$

where λ is the operating wavelength in micrometers, and the unit for α is dB/cm. The confinement loss spectrum of a plasmonic fiber sensor exhibits one or more loss peaks, corresponding to mode couplings to SPs. The loss can be monitored and measured in amplitude change at a particular wavelength. The sensitivity using the amplitude-based detection method can be defined by

$$S_A(\lambda)[\text{RIU}^{-1}] = \frac{1}{P(L, \lambda, n_a)} \frac{\partial P(L, \lambda, n_a)}{\partial n_a} = \frac{1}{\alpha(\lambda, n_a)} \frac{\partial \alpha(\lambda, n_a)}{\partial n_a}, \tag{5}$$

where α is the confinement loss, which is defined in Eq. (4), $\partial \alpha$ is the loss variation, and ∂n_a is the analyte RI variation. Amplitude interrogation requires a simple experimental setup since only intensity measurement is involved. The detection resolution is normally obtained with an assumption that 1% of transmission intensity can be detected reliably and accurately.

In addition to amplitude variation, the loss peak wavelength can also be monitored and measured for varying RI in the wavelength interrogation method. The sensitivity is defined as

$$S_\lambda[\text{nm} \cdot \text{RIU}^{-1}] = \frac{d\lambda_{\text{peak}}(n_a)}{dn_a}, \tag{6}$$

where $d\lambda_{\mathrm{peak}}$ is the shift of the wavelength of the loss peak. The detection resolution is calculated with an assumption that 0.1 nm resonance wavelength peak can be detected reliably with good accuracy. A figure of merit (FOM) takes the full width at half-maximum (FWHM) of the plasmonic peak into account, as well as the absolution resonance wavelength shift, so it provides a more comprehensive description of the sensitivity. The definition of FOM is given by

$$\mathrm{FOM} = \frac{S(\mathrm{nm/RIU})}{\mathrm{FWHM(nm)}}, \tag{7}$$

where S is the RI sensitivity obtained by wavelength interrogation, and FWHM is the full width at half-maximum of the resonance peak in the loss spectra.

Another important interrogation technique is called phase interrogation, which offers higher sensitivity but narrower detection range. The phase shift or phase difference between two polarized waveguide modes per unit sensor length is calculated by Eq. (8), and the phase sensitivity is calculated using Eq. (9):

$$\phi_d = \frac{2\pi}{\lambda}(\mathrm{Re}(n_{\mathrm{TM}}) - \mathrm{Re}(n_{\mathrm{TE}})), \tag{8}$$

$$S_\phi[\deg \cdot \mathrm{RIU}^{-1} \cdot \mathrm{cm}^{-1}] = \frac{d\phi_d(n_a)}{dn_a}, \tag{9}$$

where $\mathrm{Re}(n_{\mathrm{TM}})$ and $\mathrm{Re}(n_{\mathrm{TE}})$ are the real parts of the effective indices of the TM mode and the TE mode, respectively. The unit for the phase sensitivity is deg/RIU/cm. The peak phase sensitivity occurs in the vicinity of the resonance peak.

The optimization of the sensor performance for a particular PCF structure is carried out by varying a few key parameters, namely, metal layer thickness, size and shape of the metal wire, size of the metal NPs, and pitch and diameter of the air holes. The finite element method is commonly used for simulation studies of the sensor structure due to its capability in modeling complex structures with high spatial resolution.

The first proposal of using a PCF-based SPR sensor for RI measurement was reported by Hassani *et al.*, laying out the basis of enforcing phase-matching conditions between a plasmon and the fiber core mode using SCPCF designs [95,96]. The primary challenge was to enable a highly integrated plasmonic fiber sensor to operate in a desirable wavelength. Generally, the effective RI of a plasmon is close to that of the analyte, e.g., ~1.33 in the case of water, whereas a solid-core PCF has an effective mode index close to 1.45. In order to lower the effective index of the fiber core mode, they introduced a void in the core region so that the phase matching of the core mode and the plasmon wave can be obtained. Metallized holes with large size were introduced as the second layer of the holey cladding, forming the optofluidic channels for flowing and detecting the analyte. The schematics of the proposed fiber designs are shown in Figs. 13(a) and 13(b). Unlike a planar metalized surface that supports only one plasmonic peak, multiple plasmonic peaks in the loss spectra of the fiber core mode correspond to excitation of different plasmonic modes supported by the cylindrical metal layer. The loss spectra of the PCF structure [Fig. 13(a)] has three peaks as shown in Fig. 13(c). As the first peak is most sensitive to variation of analyte RI, it is usually used as a monitoring parameter for detecting RI change of the analyte. In addition, the sensitivity depends weakly on the gold layer thickness, as seen in Fig. 13(d). Using amplitude-based detection methods, the proposed sensor provided RI sensitivity of 10^{-4} corresponding to 1% change in the transmitted intensity.

Based on the pioneering design with a void in the core region [95], Zheng *et al.* investigated the performance of SPR sensors having silver- and gold-coated nanolayers in the PCF channels through simulation studies. The first peak in the loss spectra of the silver- and gold-coated PCFs with changing analyte RI and the respective resonance wavelength shift for RI sensitivity estimation are shown in Fig. 14. The silver-coated PCF sensor has a sharp resonance peak with a higher RI sensitivity compared to the gold-coated PCF sensor, i.e., 1167 and 984 nm/RIU, respectively. Nevertheless, the gold-coated PCF sensor exhibits better linearity in the analyte RI sensing range of 1.30–1.35 [97].

Optimization of metallic coated air holes in the second layer was proposed to enhance RI detection sensitivity. Yu *et al.* demonstrated enhanced sensor performance in a design in which selectively metallic coated air holes containing analyte channels showed an enhanced RI sensitivity up to 5500 nm/RIU [98]. Wei *et al.* proposed to have six big silver-coated air holes in the second layer and demonstrated a sensitivity of 1500 nm/RIU in simulation [99]. Another design, proposed by Akowuah *et al.*, utilized a PCF structure consisting of a central void in the core region, which was surrounded by six air holes, including two circular air holes and four elliptical air holes in the cladding, and four metalized microfluidic slots in the second layer. The cross section of the proposed design is shown in Fig. 15(a). The asymmetry of the structure resulted in birefringence in two orthogonal fundamental modes, HE_{11}^x and HE_{11}^y, with spectrally separated phase-matching wavelengths at 625 and 615 nm, respectively, as shown in Fig. 15(b) of the dispersion relation of the core guided modes

Figure 13
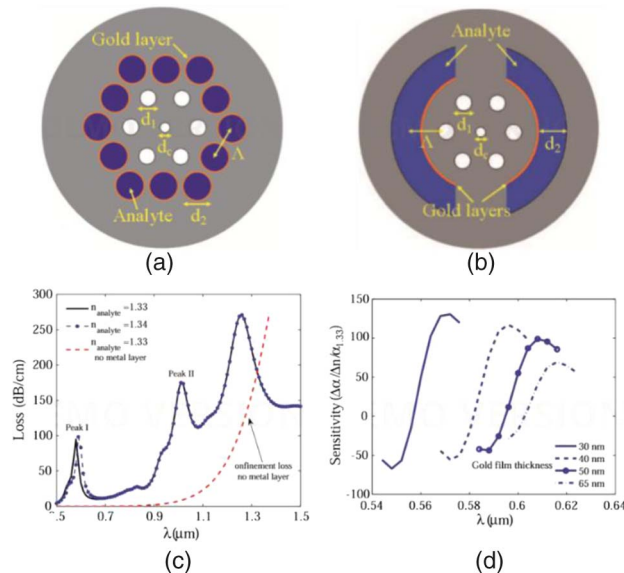
Schematics of PCF-based SPR sensors with a central void in the core region and (a) two layers of air holes in the cladding; the second-layer air holes are metal-coated and analyte filled. (b) One layer of air holes and two large metal-coated analyte filled channels. (c) Calculated loss spectra of the MOF core guided mode exhibiting three loss peaks corresponding to the excitation of various plasmonic modes in the metallized holes. Black solid line, na = 1.33; blue dotted line, na = 1.34. For comparison, the red dashed line shows the confinement loss of a core guided mode in the absence of a metal coating. (d) Sensitivity of the MOF-based SPR sensor for the 30, 40, 50, and 65 nm thicknesses of gold coating. Reprinted with permission from [95]. Copyright 2006 Optical Society of America.

and SPs. Figures 15(c) and 15(d) show the plasmonic loss peak shift when the analyte RI varied from 1.33 to 1.34. Based on simulation results, the proposed design provided different RI sensitivity for two polarizations [100]. More recently, Azzam *et al.* investigated the fundamental modes and higher order modes in the PCF structure, which were phase matched to plasmons in a similar gold-coated PCF structure. Four modes, i.e., HE_{11}^x, HE_{11}^y, HE_{12}^x, and HE_{12}^y, were analyzed to show RI sensitivities of 2200, 2400, 2200, and 2400 nm/RIU, respectively, thus confirming the proposed design's potential for multi-analyte detection [101].

Metallic film deposition on the outer side of the holey PCF was also considered for aqueous detection. Lu *et al.* reported a design based on an outer silver-coated SPR PCF sensor with RI detection resolution of $8.3 \times 10^{-5} - 9.4 \times 10^{-5}$ RIU [102]. Otupiri *et al.* optimized a PCF structure with a void in the core region, several air holes and two gold coated fluidic slots in the cladding for both the amplitude and wavelength interrogations. Both polarized core modes were considered for phase matching to plasmonic modes because of the symmetry of the gold coated layers. The sensor resolutions were $5 \times 10^{-5} - 6 \times 10^{-5}$ RIU based on wavelength interrogation and $3 \times 10^{-5} - 4 \times 10^{-5}$ RIU based on amplitude interrogation [103]. Rifat *et al.* proposed a birefringent PCF design based on outer-gold-coated SPR PCF sensor with a void in the center and demonstrated a maximum sensitivity of 4000 nm/RIU using wavelength interrogation and 320 RIU^{-1} using amplitude interrogation [104]. Further improvements of RI sensitivity in such birefringent PCFs were made by

Figure 14
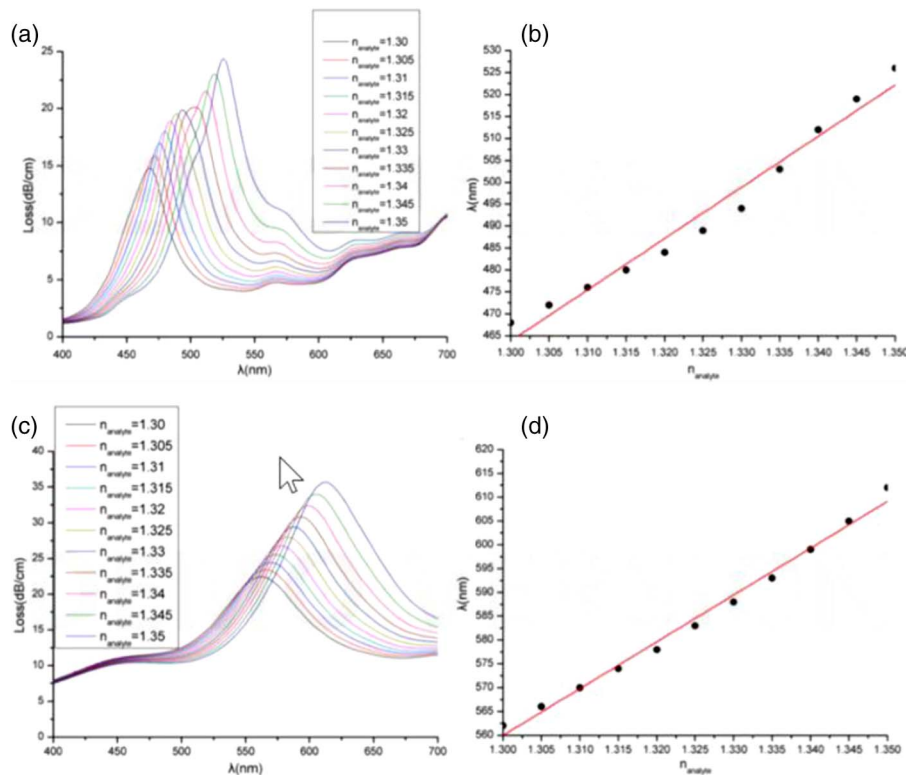
Loss spectra of the fiber core mode as a function of varying analyte RI index and the relationship between the resonance wavelength and analyte RI in (a), (b) silver-coated PCF and (c), (d) gold-coated PCF. Reprinted from Zheng *et al.*, Opt. Laser Technol. **43**, 960–964 (2007) [97]. Copyright 2010, with permission from Elsevier.

optimizing the elliptical ratio of selective air holes in the cladding. Because of the built-in high birefringence in the fiber, two polarized fundamental core modes were highly sensitive to the surrounding analyte index, showing RI sensitivities of 6700 and 1000 nm/RIU for the quasi-TM and quasi-TE modes, respectively [105]. A gold-coated D-shaped PCF with a void in the core region was optimized with the diameter of the central void as the primary variable in the analysis. It was found that increasing diameter of the central hole can improve the sensitivity in wavelength and amplitude interrogation but result in reduced phase sensitivity [106].

Near-infrared (NIR) wavelengths are favored for biosensing applications because of their deep penetration depth, as well as their commercial availability as sources and detectors. Recently, a polymer PCF coated with indium tin oxide (ITO) was proposed to acquire SPR sensing capability at the telecommunication window. The polymer substrate was PMMA. Alternate air holes in the second layer were coated by ITO and filled by analyte, and the others were air holes, as shown in Fig. 2(a). An optimized structure achieved phase matching at around 1510 nm, where mode coupling between the core and SPR modes occurred. The peak of the confinement loss coincided with the phase-matching wavelength. The phase-matching curve and the electric field profiles of the core and SPR modes are shown in Figs. 2(b)–2(d), respectively. The variation of analyte RI affected the phase-matching wavelength and confinement loss, which provided the basis for RI detection of the analyte. The results showed that RI sensitivity based on the proposed sensor was up to 2000 nm/RIU [39].

Figure 15
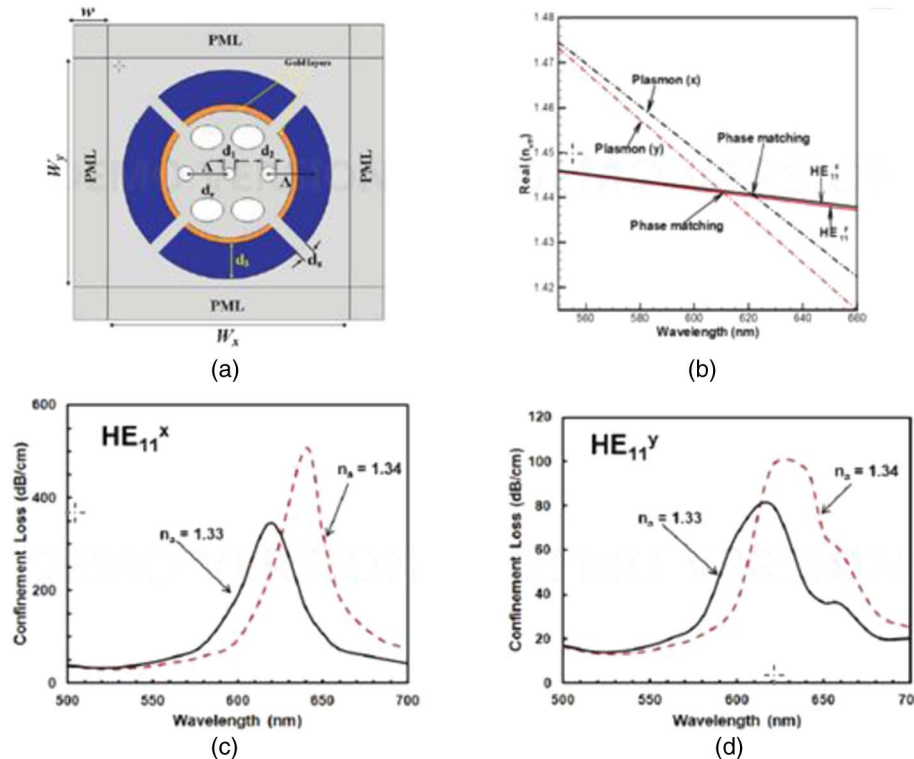
(a) Cross section of the proposed PCF design. (b) Dispersion relations of core guided modes and SPs in the vicinity of the phase-matching point of the first plasmonic peak. Caculated loss spectra of the fundamental modes (c) HE_{11}^x and (d) HE_{11}^y. © 2012 IEEE. Reprinted with permission from Akowuah *et al.*, IEEE J. Quantum Electron. **48**, 1403–1410 (2012) [100].

Designs based on SCPCFs without central voids were explored for RI sensing applications. Much effort was dedicated to improving RI detection range. Zhou *et al.* demonstrated a broadened analyte RI detection range of 1.25–1.45 with high sensitivity. The polymer PCF structure has two analyte channels arranged orthogonally in the second layer with only one channel functionalized with gold coating. Mode coupling between the solid-core mode and the SPR mode in the gold-coated analyte-filled channel occurred for RI values lower than that of the core index, while the core mode couples with the resonant mode of the adjacent analyte-filled channel for RI values higher than the core index [107]. Further broadening of detection range from 1.30 to 1.79 was reported by An *et al.* The glass material was N-LASF9. The holey cladding contained two gold-wire-filled holes and four large analyte channels [108]. Gao *et al.* presented a SPR PCF design with a germanium-doped silica core surrounded by six air holes coated with TiO_2 and gold layers. The TiO_2 film was used to enhance evanescent fields and enable spectral tuning. The RI sensitivity was $2.7 \times 10^{-5} - 5 \times 10^{-5}$ RIU [109]. The SPR resonance characteristics can be controlled by bending. Napiorkowski *et al.* demonstrated a higher degree of bend-induced tunability in plasmonic PCFs as compared to conventional optical fibers by leaking the fundamental core mode to the metal layer [110].

In addition to the aforementioned designs, other reported SCPCF structures for enhanced sensor performance include three-hole PCFs or suspended core holey fibers, grapefruit fibers filled with silver nanowires, exposed core grapefruit fibers with bimetallic structure, active PCFs, D-shaped PCFs, highly birefringent PCFs, and U-shaped PCFs.

The three-hole PCF or suspended core holey fibers were proposed for SPR sensing for liquid analyte. An auxiliary low-index dielectric layer was sandwiched between the inner wall of the PCF and the gold film deposition to optimize the overlap between the fundamental core mode and the gold layer. The proposed structure was able to achieve a refractive-index resolution of 1×10^{-4} for aqueous analytes [111]. Grapefruit fibers filled with silver nanowires were optimized to achieve RI sensitivity of 2400 nm/RIU [112]. Silver nanowires with radius of 300 nm were considered in the proposed design, and one or multiple silver nanowires were used in each grapefruit hole to generate SPR. Simulation results revealed that sensitivity was better for devices with more than one nanowire in each hole, and was stable for devices with further increase in number of nanowires. A modified grapefruit fiber structure with an exposed core was designed for SPR detection of liquid. The commercial grapefruit fiber cross section and the schematic of the exposed core grapefruit fiber are shown in Fig. 16. The core access can be obtained by polishing the grapefruit fiber, and the polished area was subsequently deposited with a thin layer of silver film. The sensor was shown to have an extremely high wavelength sensitivity of 13,500 nm/RIU for aqueous analyte over the RI range from 1.33 to 1.42 [113]. Another exposed-core PCF design was modified from the three-hole PCF [111], and a silver wire was placed in the exposed region close to the exposed core. The mode coupling between the core mode and the SP from the silver wire was utilized for RI sensing purposes, showing 2700 and 3000 nm/RIU, respectively, using wavelength interrogation, and 247 RIU^{-1} and 231 RIU^{-1} for amplitude interrogation, respectively, over a RI range of 1.33–1.34 for the two polarizations [114].

An active Yb^{3+} doped SCPCF with four large analyte channels filled with silver nanowires surrounding the core and air hole arrays in the cladding was proposed in a linear laser cavity. The sensing system was based on the measurement of the laser output power, which was influenced by the analyte RI [115].

Solid-core PCFs with a D-shaped cladding can be produced by the chemical etching or side polishing method. They allow external deposition of metallic film on a flat and smooth surface, which is easier to achieve and control compared to metallic depositions in the internal walls in PCFs in fabrication, especially compared to designs with selective metallic coating and analyte infiltration in the air holes. The aqueous analyte can be measured external to the metal-coated polished surface. Unlike PCFs with a holey cladding in a triangular lattice, An _et al._ proposed a D-shaped PCF with air holes arrayed in a rectangular lattice in the cladding layer, and a thin layer of gold film coated on the side polished surface. The proposed sensor was able to provide RI sensitivity up to 8129 and 2000 nm/RIU in RI ranges from 1.35 to 1.41 and 1.31 to 1.35, respectively [116]. Wang _et al._ optimized the gold-coated D-shaped PCF and demonstrated enhanced sensor performance up to 12,459 nm/RIU for analyte RI from 1.345 to 1.410 [117].

As an effort to achieve sharp resonance peaks and narrow spectral width, Peng _et al._ optimized a D-shaped PCF sensor with rectangular lattice and two large air holes in the first layer of a holey cladding. High sensitivity of up to 7481 nm/RIU and narrow FWHM of 13.6 nm were achieved [118]. Tan _et al._ adopted an experimental setup of phase interrogation in the sensor design, and investigated the phase shift in an all-solid D-shaped SPR PCF. The low-index rods reduced the effective index of the cladding and thus enabled a modified total internal reflection in the fiber structure. The sensor achieved a sensitivity of 9.09×10^4 degree/RIU and an improved detection limit of 2.2×10^{-6} RIU at analyte index 1.353 [119]. A comparison between phase interrogation and wavelength interrogation for an elliptical core D-shaped PCF-based plasmonic sensor was presented by Shi _et al._ It was found that the wavelength interrogation could offer a wider dynamic range and higher upper detection limit, but much lower sensitivity than obtained in phase interrogation [120].

Dash and Jha reported an ITO-coated D-shaped SPR PCF sensor for detection in the NIR region where the plasma frequency of ITO lies. The resonance wavelength of the mode coupling between the core mode and the SPR mode shifted from 1688 to 1982 nm as analyte RI varied from 1.33 to 1.37, providing RI sensitivity of 5200 nm/RIU [121]. Further improvement was demonstrated using an ITO-coated birefringent D-shaped PCF. Both wavelength interrogation and amplitude interrogation were analyzed for the structure, showing detection resolution of 17,000 nm/RIU and 74 RIU^{-1}, respectively [122]. Recently, Huang optimized the ITO-coated birefringent D-shaped PCF, and demonstrated RI sensitivities of 6000 nm/RIU,

Figure 16
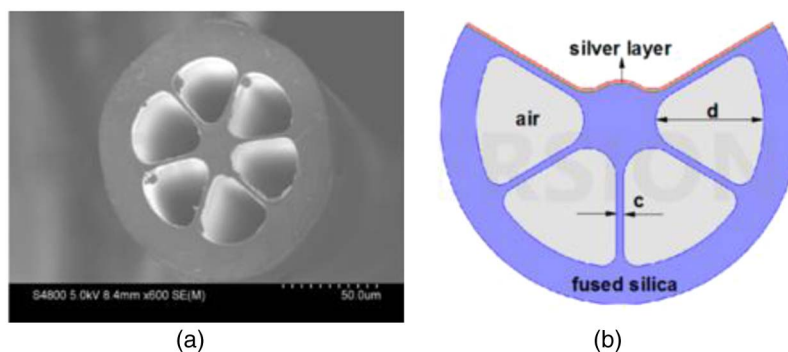
(a) Cross-section of the commercial grapefruit fiber; (b) schematic of the designed EC-GF-based SPR sensor. Reproduced from [113] under the terms of the Creative Commons Attribution 4.0 License. http://creativecommons.org/licenses/by/4.0/.

148 RIU^{-1}, and 1.2×10^6 degree/RIU/cm for the RI range from 1.30 to 1.31 by wavelength interrogation, amplitude interrogation, and phase interrogation, respectively [123].

Considering the wide adoption of highly birefringent PCF for SPR fiber sensors, Zhang *et al.* presented a detailed analysis on the suppression of polarization cross talk by large birefringence. The plasmonic PCF structure under investigation and the electric field profiles of the core modes of both polarizations are shown in Figs. 17(a)–17(c), respectively. The diameters of the air holes in the cladding and the two enlarged air holes in the first layer are d_1 and d_2, respectively. The loss spectra of the plasmonic PCF with two birefringent parameters, $d_1/d_2 = 0.95$ and 0.4 with analyte RI at 1.38 are plotted in Figs. 17(c) and 17(d) to show the polarization cross talk. Specifically, attenuation in polarized core modes and total loss were calculated. Resonance wavelength offset between polarized core modes, together with power losses, induces polarization cross talk, which will in turn lead to measurement errors. The analysis suggested that a birefringence larger than 2×10^{-4} can reduce the resonant wavelength offset to below 0.5 nm. This greatly enhances the resistance of wavelength interrogation to polarization cross talk [124]. Birefringence analysis was also proposed for locating the resonance peak, e.g., zero birefringence [125], or abrupt birefringence turning point [126], thus alleviating the need to analyze the confinement loss spectra.

Sensors based on U-shaped PCF with a rectangular lattice and gold coating on the U-type trench have been reported. The aqueous analyte detection took place in the

---

Figure 17
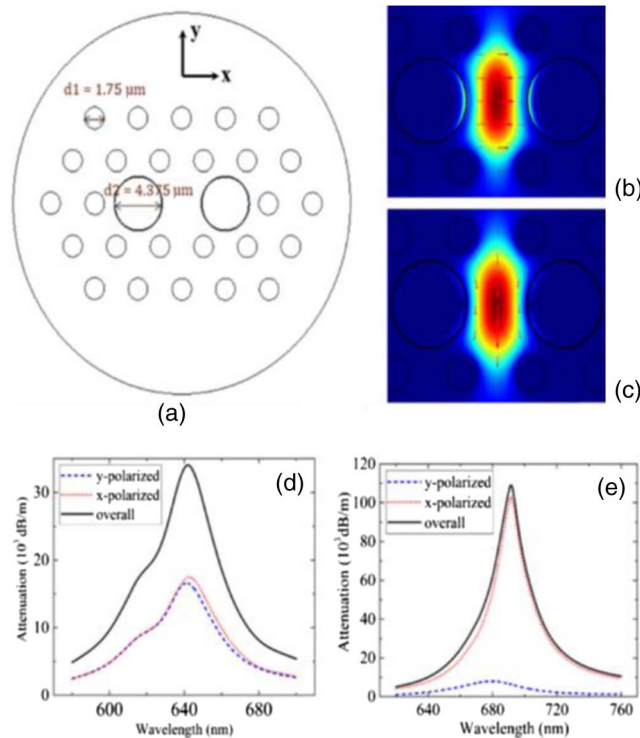
(a) Schematic structure of near-panda PCF-based SPR sensor; (b) *x*-polarized and (c) *y*-polarized core mode pattern of the proposed SPR sensor; loss spectra of PCF-based SPR sensors when (d) $d1/d2 = 0.95$ and (e) $d1/d2 = 0.4$ with analyte RI at 1.38. Reprinted from Zhang *et al.*, J. Opt. **18**, 065005 (2016) [124]. © IOP Publishing. Reproduced with permission. All rights reserved.

trench where SPR waves interacted with the analyte. Both phase interrogation and wavelength interrogation were considered for the proposed design, showing an upper detection limit at 1.384 for phase interrogation and FOM of up to 533.8 RIU^{-1} for wavelength interrogation [127].

Graphene coating has been used to prevent metallic oxidation and is also to enhance the sensing performance in plasmonic sensor construction. For examples, silver-coated or copper-coated PCF sensors with a graphene layer deposition on the metal coating have been reported for enhanced sensor performance. Dash and Jha reported a PCF structure with a void in the core region, and graphene on silver deposition on the outer layer of the fiber. Other air holes in the fiber were controlled to achieve good confinement and birefringent properties. The analyte detection occurred in the region external to the fiber structure. The sensor performance was shown to be better with higher sensitivity than a bimetallic configuration (gold on silver) [128]. The same authors reported an improved design by using a D-shaped PCF with a similar structure. RI sensitivities of 216 RIU^{-1} and 3700 nm/RIU were obtained by amplitude and wavelength interrogation, respectively, which were subsequently proposed for detection of biolayer thickness [129]. Another design was reported by Rifat *et al.*, using a PCF with triangular lattice holey cladding and three high-RI analyte-filled cores in a straight line with the central core with graphene on silver coating. Both amplitude and wavelength interrogation methods were considered, and their respective sensitivity levels were 418 RIU^{-1} and 3000 nm/RIU [130]. Yang *et al.* investigated sensor performance of a design based on an analyte-filled and graphene–silver bimetal-coated PCF with a central air hole in the core region and optimized air holes in the cladding. RI sensitivity of 2520 nm/RIU was demonstrated over a RI range of 1.33–1.34 [131]. Recently, graphene on copper deposition outside the fiber structure was considered for a plasmonic fiber sensor design. The reported PCF structure has a central void, surrounded by three layers of air holes, which can be readily produced through the standard stack-and-draw technique. The graphene-on-copper coating outside the fiber can be obtained by sputtering and the CVD deposition method. The proposed sensor was analyzed for both amplitude and wavelength interrogation, and the respective RI sensitivities were 140 RIU^{-1} and 2000 nm/RIU [132].

The void in the core region can be filled with analyte, forming a liquid core PCF as a plasmonic sensing platform especially useful for measuring analyte with RI higher than that of the host material. Zhang *et al.* compared the sensor performance of an analyte-filled core PCF with an air-filled core PCF, and demonstrated better linearization of the sensor response in a dynamic RI range of 1.33–1.42 [133]. A multi-core holey fiber design was proposed by Shuai *et al.*, with a gold-coated liquid core and holey cladding. Six silica cores were formed from six "missing" air holes in the triangular lattice. The sensor exhibited better linearity and higher sensitivity in the RI range 1.43–1.53 compared to the range 1.33–1.42, i.e., 9231 and 2929 nm/RIU, respectively [134]. Silver-coated multicore holey fiber was subsequently considered and investigated by Liu *et al.*, showing an average RI sensitivities of 4500 nm/RIU and 1013 RIU^{-1} for the RI range 1.33–1.42 using wavelength and amplitude interrogation, respectively [135].

Shuai *et al.* subsequently demonstrated that the analyte RI strongly influenced the dispersion of both the analyte-filled core mode and the plasmonic mode, resulting in the coexistence of positive and negative RI sensitivity in a multi-liquid-core-PCF-based plasmonic sensor. A cross section of the design is shown in Fig. 18(a). The fiber consists of a gold-coated core filled with analyte, and three layers of air holes in the cladding. Six holes in the second layer are also filled with analyte to form six liquid cores surrounding the metallized liquid core. This proposed sensor

exhibited different properties from the other SCPCF-based plasmonic sensors, in which the resonance peak shifted to longer wavelengths for higher RI analyte with increasing RI sensitivities. Meanwhile, the resonance wavelength experienced a red-shift for RI increasing from 1.45 to 1.495 and a blueshift for RI increasing from 1.495 to 1.53. By monitoring the peak loss of the core mode in combination with the wavelength interrogation, as shown in Fig. 18(b), the analyte RI can be determined [136]. Qin *et al.* designed a 'conjugated' PCF SPR sensor with six metalized liquid cores in the second layer of the cladding and a liquid core in the center as shown in Fig. 18(c). The change in loss spectra of the fundamental mode in the liquid core against varying analyte RI is plotted in Fig. 18(d). Two peaks were found, and they showed opposite wavelength shifts with reduced peak losses as the RI was increased from 1.46 to 1.485. Good linearity of the sensor response was obtained. The RI sensitivities of the peaks were −4354.3 nm/RIU and 2280 nm/RIU, respectively. From simulation studies, the sensor showed different sensitivities for the RI ranges of 1.485–1.50 and 1.50–1.52. The results indicated that the resonance wavelength can be fine-tuned to some desirable values through adjusting the structural parameters [137]. Instead of a triangular lattice, Gandhi et al. designed a quasicrystal fiber with an aperiodic arrangement of air holes in the cladding, a gold coated liquid core, and multiple liquid cores in the third layer of the cladding. Coexistence of positive and negative RI responses from this sensor was also observed. The maximum sensitivity was 6000 nm/RIU for low RI

Figure 18
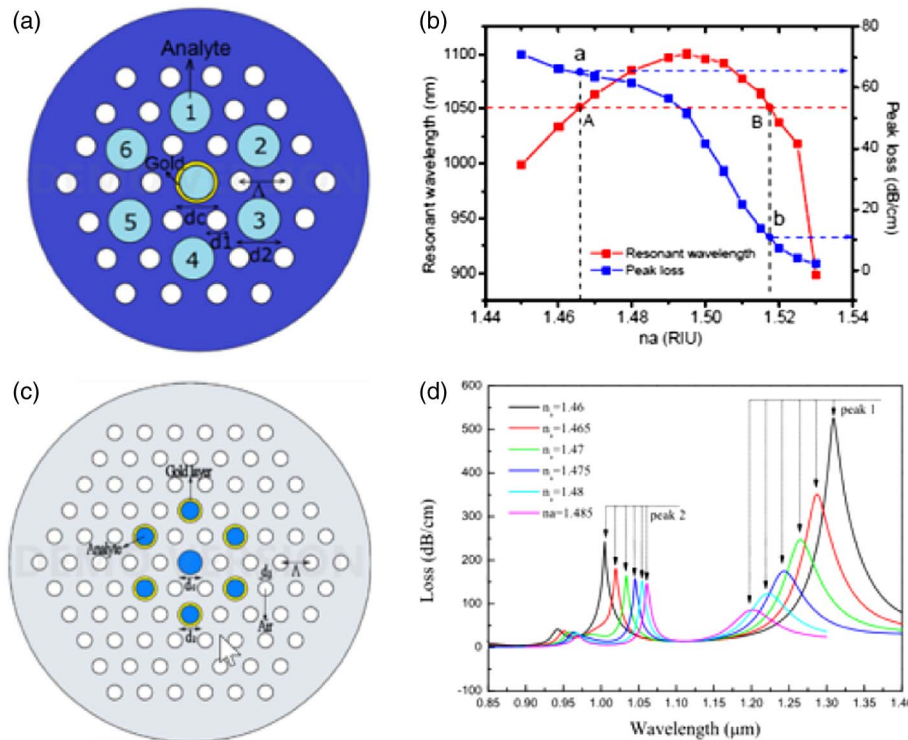
(a) Schematic of a gold-coated analyte-filled core PCF and (b) RI sensitivity by monitoring the resonance wavelength and peak loss. Reprinted with permission from [136]. Copyright 2012 Optical Society of America. (c) Cross section of the PCF SPR sensor. (d) Loss spectra of the fundamental mode for analyte RI varying from 1.46 to 1.485. Reprinted from Qin *et al.*, Opt. Laser Eng. **58** 1–8 (2014) [137], Copyright 2014, with permission from Elsevier.

range 1.45–1.46 and −4000 nm/RIU for high RI range 1.52–1.53 [138]. Fan *et al.* reported further improvements in sensitivities and provided a comparison of sensor performance between gold-coated and silver-coated fiber sensors. The PCF sensor has an analyte core surrounded by three layers of air holes in the cladding and two metalized cores in the second layer. For an RI range of 1.40–1.42, the gold-coated sensor design showed slightly higher RI sensitivity, i.e., −7040 nm/RIU and −7017 nm. Nevertheless, the silver-coated sensor exhibited a sharper loss peak and a better FOM, i.e., 73.8 RIU^{-1} and 5.9 RIU^{-1} at 1.40 RIU, respectively [139]. Tan *et al.* used a different approach compared to previous reports, by filling liquid with controllable RI into the hollow core of a D-shaped PCF, which allowed deposition of gold film and subsequent analyte detection external to the fiber structure. The proposed sensor offered an effective way of tailoring the core mode while maintaining the simplicity and robustness of analyte detection. The best sensitivity was found to be 3350 nm/RIU for the analyte RI range 1.33–1.34 with filling liquid with RI of 1.39. Further improvement in sensitivity was possible with filling with a high-dispersion liquid [140].

Photonic bandgap PCF-based SPR sensors were studied and optimized for sensing aqueous solutions in the visible and NIR [141,142]. Several bandgap fiber structures were discussed and analyzed for SPR RI sensing, including solid-core Bragg-fiber-based SPR sensors with large or small core size, analyte-filled hollow-core Bragg-fiber-based SPR sensors, and honeycomb PCF-based SPR sensors. The schematics of the fiber structures are shown in Fig. 19. The bandgap guidance enables flexibility in designing any desirable operating wavelength from the visible to NIR. Based on simulation results, sensor resolutions in the range $7 \cdot 10^{-6} - 5 \cdot 10^{-5}$ RIU were demonstrated for an aqueous analyte.

Tian *et al.* reported a detailed analysis of an all-solid D-shaped PCF structure by looking at the effect of several parameters, including the silver coating thickness, first layer

---

Figure 19
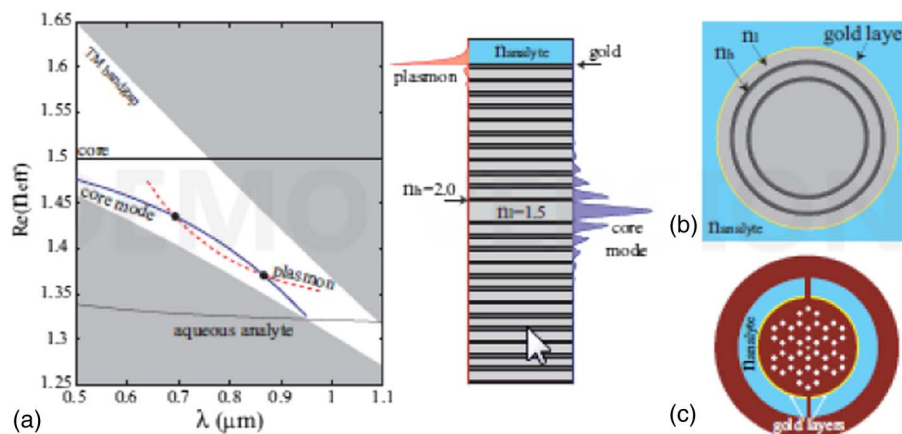
Schematics of photonic-crystal waveguide-based SPR sensor schemes. (a) Single-mode planar photonic-crystal-waveguide-based SPR sensor. The dispersion relation of the core guided mode is in solid blue; that of the plasmon is in thick dashed red. Inset: coupler schematic; |Sz| of a plasmon (left) and a core mode (right). (b) Solid core Bragg-fiber-based SPR sensor. (c) Microstructured core, honeycomb photonic-crystal-fiber-based SPR sensor. Reprinted with permission from [141]. Copyright 2007 Optical Society of America.

rods, and polishing depth on sensor performance. It should be noted that the guiding mechanism in this design was also based on the photonic bandgap effect [143].

A performance comparison among reported designs of plasmonic PCF schemes based on their structures for aqueous analyte RI detection is summarized in Table 4. Due to the high loss of the plasmonic fibers based on metal coatings, e.g., ranging from below 100 to 8000 dB/cm, photon propagation is limited to a few hundred micrometers. Therefore, this kind of sensor should be considered and developed only as an integrated photonic element rather than a fiber [95]. Some designs have relatively lower loss, e.g., below 20 dB/cm, with light propagation of a few millimeters in the structure for sensing purposes and allowing practical fiber handling, such as cleaving and splicing [140,141]. The design of an exposed core PCF embedded with a single metal nanowire has been shown to offer similar sensitivities compared to metal-coated PCF sensors, but with much reduced losses, e.g., 1–5 dB/cm for both polarizations [114]. Therefore, the schemes based on nanowire embedded PCFs and metal-coated PCFs, which have lower loss values, should be explored further for sensing applications in light of their high chance for practical realization.

4.2. Dual- or Multi-Analyte Sensing

Multichannel analyte detection by SPR sensors has witnessed development similar to that of SPR sensors for single analyte detection, from bulk prism-coupled configurations to miniaturized fiber optic structures (references on multi-analyte by previous effort). The presence and flexible design of air hole channels enables feasible developments for dual- or multi-analyte sensing in PCF-based plasmonic devices, which are favored for many applications, such as clinical diagnostics, drug discovery, and environmental monitoring.

The first PCF-based multichannel plasmonic sensor was proposed by Zhang *et al.* in 2011 [144]. Similar to an earlier proposed three-hole PCF structure [111], the proposed design introduced modifications of multilayers, e.g., cladding layers with lower RI than silica were introduced and, subsequently, gold layers were deposited uniformly. An overlay layer was introduced on gold coating in channels for sensing purposes. Dual-analyte detection was proposed by incorporating two types of sensing layers in the channels, so that channels with different sensing layers exhibited a spectrally differentiable plasmonic loss peak. The numerical results showed average RI sensitivity of 1535 nm/RIU over a RI range of 1.33–1.36 for all channels [144].

Another multichannel plasmonic PCF design was proposed by Otupiri *et al.*, with a central void in the core region, surrounded by four rotated elliptical air holes in the first layer and four large gold-coated analyte-filled channels in the second cladding layer. Two channels in the horizontal axis were also coated by a Ta_2O_5 overlayer underneath the gold-coating layer. The Ta_2O_5 and gold-coated channel pair were denoted as channel 1 and the gold-coated channel pair were denoted as channel 2, which were filled by different analytes. Two plasmonic loss peaks were found and attributed to phase matching between core guide modes and plasmons at channels 1 and 2 for both polarizations. The phase-matched wavelengths for the *x*-polarized fundamental mode were 675 and 900 nm, and were 645 and 836 nm for the *y*-polarized fundamental mode. It was found that the *x*-polarized mode had a dominant plasmonic loss peak due to channel 1, whereas the *y*-polarized mode had a dominating peak due to channel 2. By detecting the wavelength shifts of the two plasmonic peaks, dual analyte RI in either channel can be measured. The wavelength interrogation method was used for the dual-analyte detection mode, showing sensor sensitivities up to 4600 nm/RIU and 2300 nm/RIU for the *x*-polarized and *y*-polarized modes, respectively. In addition, the sensor can be operated in a self-referencing mode, i.e., in one channel the analyte

Table 4. Simulated Performance of Metal-Coated Plasmonic PCF Sensors Based on SPR for Aqueous Analyte RI Detection

PCF Characteristics	RI Range	Interrogation	Sensitivity[a]	Loss[b] (dB/cm)	Resolution (RIU)[c]	FOM(RIU^{-1})	References
Solid core PCF with a void in the core region							
Au-coated	1.33–1.34	Amplitude	100	~180	10^{-4}	—	Hassani 2006 [95]
Au-coated	1.30–1.35	Wavelength	1167	~30	8.57×10^{-5}	—	Zheng 2011 [97]
Ag-coated			984	~40	1.02×10^{-4}	—	
Au-coated	1.331.34	Amplitude	HE_{11}^x:220	~400	4.54×10^{-5}	—	Akowuah 2012 [100]
		Wavelength	HE_{11}^y:125	~80	8×10^{-5}		
			HE_{11}^x:2000		5×10^{-5}		
			HE_{11}^y:1500		6.67×10^{-5}		
Au-coated	1.33–.134	Wavelength	HE_{11}^x:2200	>1000	4.54×10^{-5}	—	Azzam 2016 [101]
			HE_{11}^y:2400		4.17×10^{-5}		
			HE_{12}^x:2200		4.54×10^{-5}		
			HE_{12}^y:2400		4.17×10^{-5}		
Au-coated	1.37–1.41	Wavelength	5500	~100	10^{-5}	73	Yu 2009 [98]
Ag-coated	1.325–1.345	Wavelength	1500	~140	6.67×10^{-5}	—	Wei 2012 [99]
Ag-coated	1.33–1.335	Wavelength	1064–1205	~120	$8.3 \times 10^{-5} - 9.4 \times 10^{-5}$	—	Lu 2013 [102]
Au-coated	1.33–1.34	Wavelength	1667–3333	~700	$3 \times 10^{-5} - 6 \times 10^{-5}$	—	Otupiri 2014 [103]
Au-coated	1.33–1.37	Amplitude	320	~50	3.13×10^{-5}	—	Rifat 2015 [104]
		Wavelength	4000		2.5×10^{-5}		
Au-coated	1.33–1.34	Amplitude	HE_{11}^x:519.4	~100	1.925×10^{-5}	—	Hameed 2016 [105]
		Wavelength	HE_{11}^y:631.5	~50	1.583×10^{-5}		
			HE_{11}^x:10^4		1×10^{-5}		
			HE_{12}^y:6700		1.49×10^{-5}		
Au-coated	1.34–1.48	Wavelength	1131	~100	8.84×10^{-5}	—	Liu 2016 [126]
D-shaped and Au-coated[d]	1.33–1.34	Amplitude	120	~2000	8.3×10^{-5}	—	Luan 2015 [106]
		Wavelength	2900		3.4×10^{-5}		
		Phase	5.30×10^4		—		
Solid core PCF without a central void							
ITO-coated	1.33–1.35	Amplitude	80	~1750	12×10^{-5}	—	Dash 2014 [39]
		Wavelength	2000		5×10^{-5}		
Au-coated	1.25–1.383	Wavelength	1.4×10^4	>360	7.1×10^{-6}	—	Zhou 2012 [107]
	1.383–1.45		2.7×10^4		3.7×10^{-6}		
Au wire	1.30–1.63	Wavelength	100	~2500	1.0×10^{-4}	—	An 2016 [108]
	1.63–1.79		3233		3.09×10^{-5}		
TiO$_2$ and Au-coated	1.33–1.35	Amplitude	370	~60	2.7×10^{-5}	—	Gao 2014 [109]
		Wavelength	2000		5×10^{-5}		

(Table continued)

Table 4. Continued

PCF Characteristics	RI Range	Interrogation	Sensitivity[a]	Loss[b] (dB/cm)	Resolution (RIU)[c]	FOM(RIU^{-1})	References
Three-hole PCFs Au-coated	1.33–1.34	Amplitude	80	~70	1.25×10^{-4}	—	Hautakorpi 2008 [111]
		Wavelength	1000		1×10^{-4}		
Grapefruit fibers Ag nanowire	1.33–1.335	Wavelength	2400	~700	4.17×10^{-5}	—	Lu 2012[112]
Exposed core grapefruit fibers	1.33–1.42	Amplitude	HE^x_{11}:204	~8000	4.9×10^{-5}	—	Yang 2015 [113]
Ag-coated		Wavelength	HE^y_{11}:191	~1000	5.23×10^{-5}		
			HE^x_{11}: up to 13500 (not linear)		7.4×10^{-6}		
			HE^y_{11}: up to 12,000 (not linear)		8.3×10^{-6}		
Exposed core three hole fiber Ag wire[e]	1.33–1.34	Amplitude	HE^x_{11}:247	5	4.05×10^{-5}	—	Luan 2016 [114]
		Wavelength	HE^y_{11}:231	1	4.33×10^{-5}		
			HE^x_{11}:2700		3.70×10^{-5}		
			HE^y_{11}:3000		3.33×10^{-5}		
D-shaped SCPCF without a central void							
Au-coated	1.33–1.35	Wavelength	2000	~100	5×10^{-5}	—	An 2014[116]
	1.35–1.41		8129	~300	1.23×10^{-5}		
Au-coated	1.37–1.398	Wavelength	7481	~400	1.34×10^{-5}	478.3	Peng 2015 [118]
Au-coated	1.333–1.357	Phase	6.5×10^4	~100	2.2×10^{-6}	—	Tan 2014/ [119]
Au-coated	1.36–1.41	Wavelength	6000	~1000	1.67×10^{-5}	—	Shi 2015 [120]
	1.371–1.373	Phase	2.2×10^5		—		
ITO-coated	1.33–1.37	Wavelength	5200	~140	1.92×10^{-5}	—	Dash 2016 [121]
ITO-coated	1.33–1.35	Amplitude	74	~40	1.35×10^{-4}	—	Dash 2016 [122]
		Wavelength	1.7×10^4		5.8×10^{-6}		
ITO-coated	1.30–1.31	Amplitude	148	~1000	6.76×10^{-5}	—	Huang 2016 [123]
	1.28–1.34	Wavelength	6000		1.67×10^{-5}		
	1.28–1.34	Phase	1.2×10^6		—		
Highly birefringent PCFs							
Au-coated	1.33–1.38	Wavelength	3000	~90	3.33×10^{-5}	—	Zhang 2016 [124]
U-shaped PCFs	1.365–1.395	Wavelength	$\sim 7.6 \times 10^3$	~150	1.32×10^{-5}	533.8	Ge 2016[127]
	1.382–1.384	Phase	8.1×10^4		—		
Graphene-coated PCFs							
Graphene on silver	1.33–1.37	Amplitude	860	~1500	1.16×10^{-5}	—	Dash 2014 [128]
Graphene on silver	1.33–1.37	Amplitude	216	~200	4.6×10^{-5}	—	Dash 2015 [129]
		Wavelength	3700		2.7×10^{-5}		
Graphene on silver	1.46–1.49	Amplitude	418	~100	2.39×10^{-5}	—	Rifat 2015 [130]
		Wavelength	3000		3.33×10^{-5}		
Graphene on silver	1.33–1.34	Wavelength	2520	~100	3.97×10^{-5}	—	Yang 2016 [131]

(Table continued)

Table 4. Continued

PCF Characteristics	RI Range	Interrogation	Sensitivity[a]	Loss[b] (dB/cm)	Resolution (RIU)[c]	FOM(RIU^{-1})	References
Graphene on copper	1.33–1.37	Amplitude	140	~50	7.14×10^{-5}	—	Rifat 2016 [132]
		Wavelength	2000		5×10^{-5}		
LCPCFs							
Au-coated	1.33–1.42	Wavelength	4200	~550	2.38×10^{-5}	—	Zhang 2011 [133]
			2600		3.85×10^{-5}		
Au-coated	1.33–1.42	Wavelength	2929	~32	3.41×10^{-5}	—	Shuai 2012 [134]
			9231		1.08×10^{-5}		
Ag-coated	1.43–1.53	Amplitude	1013	~25	9.87×10^{-5}	—	Liu 2015 [135]
		Wavelength	4500		2.22×10^{-5}		
Au-coated	1.45–1.46	Wavelength	3700	~70	2.7×10^{-5}	—	Shuai 2012 [136]
	1.52–1.53		−5500		1.82×10^{-5}	98.2	
Au-coated	1.45–1.49	Wavelength	6000	~0.04	1.67×10^{-5}	—	Gandhi 2016 [138]
	1.5–1.53		−4000		2.5×10^{-5}		
Au-coated	1.46–1.485	Wavelength	−4354.3	~500	2.3×10^{-5}	79.2	Qin 2014 [137]
	1.485–1.50		−3800		2.63×10^{-5}	—	
	1.50–1.52		−4240		2.36×10^{-5}	—	
Ag-coated	1.40–1.42	Wavelength	−7017	~700	1.43×10^{-5}	73.8	Fan 2015[139]
Au-coated		Wavelength	−7040	~200	1.42×10^{-5}	5.9	
Au-coated	1.38–1.46	Wavelength	3350	~7	2.99×10^{-5}	—	Tan 2014 [140]
Bandgap PCFs							
Au-coated large solid-core Bragg fiber	1.33–1.34	Amplitude	214	~8	4.7×10^{-5}	—	Gauvreau 2007 [141]
		Wavelength	1900		5.3×10^{-5}		
Au-coated small solid-core Bragg fiber		Amplitude	293	~5	3.4×10^{-5}	—	
		Wavelength	1020		9.8×10^{-6}		
Au-coated analyte filled Bragg fiber		Amplitude	365	~80	2.7×10^{-5}	—	
		Wavelength	7000		1.4×10^{-5}		
Au-coated honeycomb PCF		Amplitude	400	~250	2.5×10^{-5}	—	
		Wavelength	13750		7.2×10^{-6}		
Ag-coated all solid bandgap fiber	1.33–1.38	Wavelength	7300	~60	1.37×10^{-5}	216	Tian 2012 [143]

[a]The units of sensitivity are RIU^{-1}, nm/RIU, and deg/RIU/cm for amplitude, wavelength, and phase interrogation, respectively. Unless otherwise specified, the sensitivity is calculated for the HE_{11}^y mode.

[b]It is highly dependent on the order of the plasmonic peak, the metal layer thickness, the fiber geometry, and the RI of the analyte. The loss at the first peak of SPR resonance for the lowest RI value in the detection range is included in the table. In addition, the value of the loss is indicative only as it varies with different metal layer thickness.

[c]The resolution is calculated by assuming that 1% of change in the transmitted intensity or a 0.1 nm change in resonance wavelength can be accurately and reliably detected in amplitude or wavelength, respectively.

[d]The diameter of the central hole is fixed at 0.2Λ in the structure for the three interrogation methods.

[e]This work about a nanowire embedded PCF is included in the table to show the difference in loss as compared to metal-coated PCF sensors.

[f]The sensor length was 1.4 cm to provide a 130 dB loss in the sensing region; a noise level of 0.2 deg was assumed for the sensor.

was fixed, and changes in analyte RI can be measured in the other channel. The amplitude interrogation method was used for the self-referencing mode with RI sensitivities of 425 RIU^{-1} and 131 RIU^{-1} for the *x*-polarized and *y*-polarized modes, respectively [145].

4.3. Temperature Sensing and Dual Parameter Sensing

The high RI sensitivity of plasmonic PCF sensors has motivated researchers in designing and developing plasmonic PCF sensors for sensitive temperature measurement. In 2007, Florous *et al.* proposed to incorporate gold NPs in a PCF for temperature sensing. The PCF had a solid core surrounded by two layers of air holes. The localized surface plasmons (LSPs) excited by the propagating core mode can be temperature tuned as the gold NPs are heated or cooled to result in a wavelength shift in the plasmonic peak. Numerical simulations demonstrated the temperature sensitivities of spherical and ellipsoidal gold-NP-deposited PCF sensors, showing 0.062 nm/°C and 0.046 nm/°C, respectively [146]. The gold NP deposition can be achieved by techniques discussed in Section 3.3.

To enhance the temperature sensitivity, a liquid with a high thermo-optic coefficient can be used to completely or selectively fill air holes in the PCFs to induce temperature dependence of the plasmonic response. Depending on the interrogation method of the sensors, the temperature sensitivity can be evaluated by measuring the amplitude, wavelength, or phase of the plasmonic resonance.

Silver-nanowire-filled PCFs were proposed for temperature sensing [147,148,57]. The air holes were filled with a mixture of ethanol and chloroform, with high thermo-optic coefficients of -6.328×10^{-4} and -4×10^{-4}, respectively. By controlling the mixing volume ratio for the infiltration into the air holes of the PCF structure, the desirable temperature sensing range can be tuned. Luan *et al.* proposed a temperature sensor based on a grapefruit PCF filled with silver nanowires. The calculated temperature sensitivity was around 4 nm/°C [147]. The influence of the shapes of silver nanowires was studied by Wang *et al.*, using an octagon PCF structure. Three shapes were considered in the simulation, i.e., circle, ellipse, and square, showing temperature sensitivities of 0.25, 0.4, and 0.2 nm/°C from $-40 - 0$°C, respectively [148]. Yang *et al.* reported both theoretical and experimental investigation of silver-nanowire-filled large mode area (LMA) PCF-based SPR sensor for temperature sensing. Using a commercially available LMA-10 PCF structure as the sensor platform, the mixing volume ratio of ethanol and chloroform was varied from 1:1 to 1:3, resulting in a redshift of peak wavelength as well as an increase in peak loss for the temperature range 25°C–60°C. The experimental results confirmed high temperature sensitivity up to -2.0833 nm/°C with an FOM of 0.1572°C^{-1} [57].

In 2012, Peng *et al.* reported a temperature sensor based on a selective coated SPR PCF. The PCF design contained a void in the central core region, surrounding by two layers of air holes. The second layer of air holes with larger diameters were filled with a sensing medium with large thermo-optic coefficient, i.e., -4×10^{-4}, and selectively coated by gold. Numerical calculations suggested a spectral sensitivity of 0.72 nm/°C of the proposed sensor for a 0°C–50°C detection range. The gold film thickness played an important role in influencing the FWHM of the loss resonance peaks, while the sensitivity remained stable. Consequently, the FOM obtained by thinner gold film was higher. An optimal coating thickness of 35 nm was suggested by considering the sensor length, loss dynamic range, and the FOM [149]. A multi-core PCF with a gold-coated liquid-filled core was proposed for temperature sensing, achieving good linearity of 0.99991, high sensitivity of -2.15 nm/°C, and average FOM of -0.044°C^{-1} in the range of 20°C–80°C [150]. More recently, Hameed *et al.* explored

Table 5. Performance of the Plasmonic PCF Temperature Sensors

PCF Characteristics	Thermo-Optic Coefficient ($°C^{-1}$)	Temperature Range (°C)	Sensitivity (nm/°C)	FOM ($°C^{-1}$)	References
Solid core PCF with Au NP deposition on the inner wall of the air holes	—	−173.15–226.85	0.062 (Spherical) 0.046 (Ellipsoidal)	—	Florous 2007 [146]
Selectively Au-coated PCF with a central void	-4×10^{-4}	0–50	0.72	0.013–0.026	Peng 2012 [149]
Multi-core PCF with an Au-coated liquid core	-4.65×10^{-4}	20–80	−2.15	−0.044	Liu 2015 [150]
Grapefruit PCF with six holes filled with Ag nanowires	Ethanol -6.328×10^{-4} Chloroform -4×10^{-4}	−4–15	4	—	Luan 2014 [147]
Octagon PCF filled with Ag nanowires	Ethanol -6.328×10^{-4} Chloroform -4×10^{-4}	−40–0	0.25 (Circle) 0.5 (Ellipse) 0.4 (Square)	—	Wang 2015 [148]
LMA PCF filled with Ag nanowires	Ethanol -6.328×10^{-4} Chloroform -4×10^{-4}	25–60	−2.08	0.135–0.1572	Yang 2016 [57]
LCPCF with Au nanowire	Temperature-dependent Cauchy coefficient for NLC E7 [155]	30–50	10	—	Hameed 2016 [153]
Ag-coated exposed core PCF with one Ag coated and liquid filled channel	Ethanol -6.328×10^{-4} Chloroform -4×10^{-4}	26–43	6.18	—	Luan 2016 [154]

the combination of nematic liquid crystal (NLC), which is highly temperature dependent, and PCFs filled with nanowires for temperature sensing. Compared with NLC-filled PCF devices without plasmonic couplings [151,152], the proposed NLC core SPR PCF design offered a higher temperature sensitivity as well as broader sensing range with linear response [153]. The temperature dependence of the NLC was described by the Cauchy coefficient [155].

Dual parameter sensing is an important and desirable capability especially for the purpose of differentiating the parameters or minimizing cross talk, e.g., RI and temperature. Most plasmonic PCF sensors for liquid analyte measurement with high RI sensitivity are prone to temperature-induced cross talk. To address this challenge, Luan *et al.* used an exposed-core PCF with silver layers coated on the exposed core and one air hole next to the core for dual parameter sensing. In the proposed design, a liquid mixture of ethanol and chloroform was filled in the silver-coated air hole, which was responsible for the temperature sensing; the RI of the liquid analyte was measured external to the silver-coated exposed core. Two resonance peaks were present for both orthogonal polarizations, with a major peak at 838 nm for the *x*-polarized mode supported by the temperature sensing channel, and a major peak at 535 nm for the *y*-polarized mode supported by the RI sensing channel. Each peak was shifted by temperature or variation of the analyte RI. The proposed sensor exhibited RI sensitivity of 1900 nm/RIU for the RI range 1.33 to 1.34, and temperature sensitivity of 6.18 nm/°C for temperature range 26°C–43°C [154]. A summary of the plasmonic PCF sensors for temperature measurement is shown in Table 5.

4.4. Polarization and Birefringent Devices

Plasmonic PCFs exhibit high losses in the core modes at phase-matched wavelengths due to strong power coupling to SPP modes, inviting substantial interest and effort in developing fiber filter devices at specific communication wavelengths or broadband communication windows. Various designs of plasmonic PCF structures incorporating metal wires, coatings, or NPs are reviewed based on the type of metal configuration and PCF characteristics in this section.

4.4a. Metal-Wire-Filled PCFs

Mode coupling between two orthogonal polarization directions in plasmonic PCFs was studied for polarization splitting by Nagasaki *et al.* Their work investigated the polarization-dependent loss characteristics in a gold-wire-filled SCPCF with a triangular lattice of air holes in the cladding. The core mode could be coupled only to second or higher order SPPs. It was found that PCFs with a single gold wire showed similar loss peak wavelengths and loss values for both polarizations. In contrast, PCF structures with several gold wires selectively filled some air holes were achieving the high polarization extinction ratio desirable for polarization filter applications. The arrangement of the gold wires played an important role in the fiber's polarization dependence. In addition, the diameter of the gold wires was increased to achieve a large polarization extinction ratio over a wide range of wavelengths [38]. The birefringence is a key parameter to decrease the coupling length between the two orthogonal polarization states in order to enhance the polarization splitting. A polarization-maintaining (PM) PCF with a triangular lattice of air holes in the cladding and one gold wire filled into one air hole was studied by Du *et al.* The study revealed the relative significance of design parameters, namely, gold wire positions, gold wire dimension, birefringence strength, and pitch of air holes, on the polarization splitting ratio. By optimizing the fiber geometry and the inclusion of two gold wires in the cladding, complete separation of two polarization-dependent plasmonic resonances was demonstrated, thereby making it possible to realize polarization splitting filters operating at communication wavelengths. Two designs were proposed for polarization-dependent wavelength filters, as shown in Figs. 20(a) and 20(b) [156]. A D-shaped PM PCF with a gold nanowire, as shown in Fig. 20(c), was used as a polarization filter. The device was operating at communication wavelengths, i.e., 1310 and 1550 nm, with cross talk better than 30 dB and bandwidths at 88 and 150 nm, respectively [157]. Yogalakshmi *et al.* reduced the diameter of air holes in the inner two layers compared to that of the outer two layers, and demonstrated polarization filtering by controlling the number of gold wires and changing the positions of the gold nanowires. In addition, gold coatings were used to tune to the desirable peak resonance wavelength and control the absorption loss factor [158]. Silver–gold alloys have been proposed for developing plasmonic devices, utilizing the flexibility of controlling the composition to obtain a desirable plasmonic resonance wavelength [159]. More recently, tunable narrowband polarization filters were designed based on PCFs with a solid core, and the first layer air holes were filled by liquid crystal in the cladding, and a liquid crystal core or a liquid core surrounded by a triangular lattice of air holes and gold wires in the cladding. The tunability was achieved by temperature tuning [160], applying an external electrical field to control the rotation angle of the liquid crystal, as shown in Fig. 20(d) [161] or changing the filled liquid [162].

PCFs with air holes in a square lattice and filled with metal wires have received significant attention for the development of polarization filtering devices. Zhang *et al.* showed that the size of the gold wire and the symmetry of the air holes around the solid core have significant impact on the polarization filtering characteristics. An optimized design with two gold nanowires in the cladding was demonstrated for peak loss up to 279.10 and 399.18 dB/cm at wavelengths of 1.02 and 1.55 μm, respectively [163]. By adjusting the gold wire diameter, An *et al.* proposed a PCF design with a solid core surrounded by air holes in a square lattice and two gold wires for a polarization filter at communication wavelengths of 1310 and 1500 nm [164]. Jiang *et al.* designed an ultrashort PCF single polarization wavelength filter of 0.3 mm for communication wavelengths of 1310 and 1500 nm. The PCF was filled with a single gold wire next to the solid core in the holey cladding in a square lattice. A cross section of the fiber design and the dispersion as well as the modal loss is presented in Fig. 21.

Fiber core modes were coupled to second-order SPP modes in orthogonal polarizations, resulting in completely separated polarization loss peaks at two wavelengths [165]. An ultra-broadband single polarization filter was reported by the same group using a PCF with a liquid crystal core and filled with a single gold wire in the square lattice holey cladding. Simulations suggested that the design was able to achieve high polarization extinction ratio in 1.25–2.1 µm, which is desirable for broadband single polarization filter applications [166]. A spiral PCF with an elliptical core and filled with gold wires were investigated by Heikal *et al.* The study showed that by changing the structural parameters and the number of gold wires, the coupling between core modes and higher order SPP modes can be controlled, offering opportunities for designing polarization-dependent wavelength filters [167]. The performance figures of the polarization-dependent wavelength filters based on the proposed plasmonic PCF with different holey patterns in the cladding and filled with metal wires are summarized in Table 6.

Dual core PCFs with gold nanowires have been widely explored for achieving polarization filtering characteristics utilizing the difference in resonance coupling character-

Figure 20
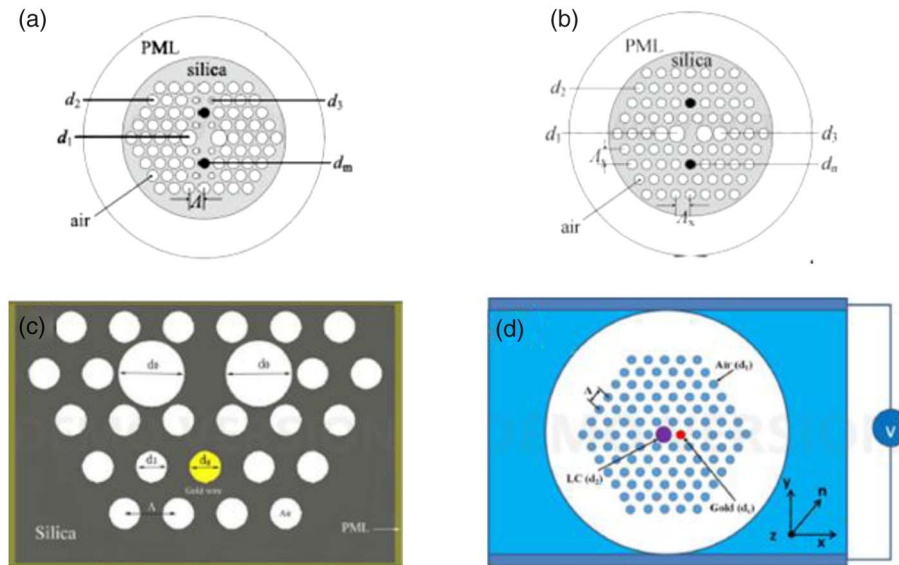
Examples of SCPCF with triangular lattice and filled with metal wires for polarization filter devices. (a) Schematic diagram of the simple designed HB-PCF. Diameters of the two big air holes, the eight small air holes, and the other air holes are $d_1 = 2.6$ µm, $d_3 = 1.0$ µm and $d_2 = 1.9$ µm. The pitch between the adjacent air holes is 2.4 µm. The diameters of the two filling gold wires are $d_m = 1.7$ µm. (b) Schematic diagram of the specially designed HB-PCF. The diameters of the two big air holes, the second big air holes and the other air holes are $d_1 = 2.6$ µm, $d_2 = 2.2$ µm and $d_3 = 1.6$ µm. The diameters of the two filling gold wires are $d_m = 1.6$ µm. The pitch between the adjacent air holes in the horizontal direction is 2.4 µm. Reprinted from Du *et al.*, Appl. Phys. B **109**, 65–74 (2012) (Figs. 7 and 9) [156]. Copyright © 2012, Springer-Verlag. (c) Schematic diagram of the designed D-PCF with gold nanowire. Reprinted with permission from Fan *et al.*, Plasmonics **10**, 675–682 (2015) (Fig. 1) [157]. Copyright © 2014, Springer Science+Business Media New York. (d) Cross section of the PLC-PCF filter filled with a metal wire and sandwiched between two electrodes. Reprinted with permission from [161]. Copyright © 2015 Optical Society of America.

istics of even and odd supermodes, high birefringence, and high polarization dependence in transmission [168–176]. In a dual core PCF structure, the extinction ratio is defined as the power ratio between the undesired and the desired polarization states in each output port or core.

Zhang *et al.* used supermode theory and the coupled mode theory to confirm the enhancement of the power transfer between two fiber cores due to the presence of a silver wire in between and its associated resonant coupling between SPs and fiber core modes. The coupling characteristics of a gold-wire-filled and gold-coated PCF coupler were investigated, showing a coupling ratio of up to −30.54 dB between two fiber cores [168]. Li *et al.* investigated the difference in resonance coupling characteristics, dispersion, and confinement loss properties for the even and odd supermodes in a dual core PCF with gold wire in between the two cores. Polarization-dependent transmission was demonstrated, and two orthogonally polarized components can be separated in the proposed gold-filled dual core PCF coupler. Specifically, at 1330 nm, the light in one core was purely *x*-polarized and the other core was purely *y*-polarized after an optimized propagating length; the power ratio of the orthogonal polarizations in each core was around −40 dB [169]. A polarization splitter was demonstrated using a silver-wire-filled dual core PCF of 63 mm length. The polarization splitting was achieved by designing a dual core plasmonic PCF with coupling length ratio of

Figure 21
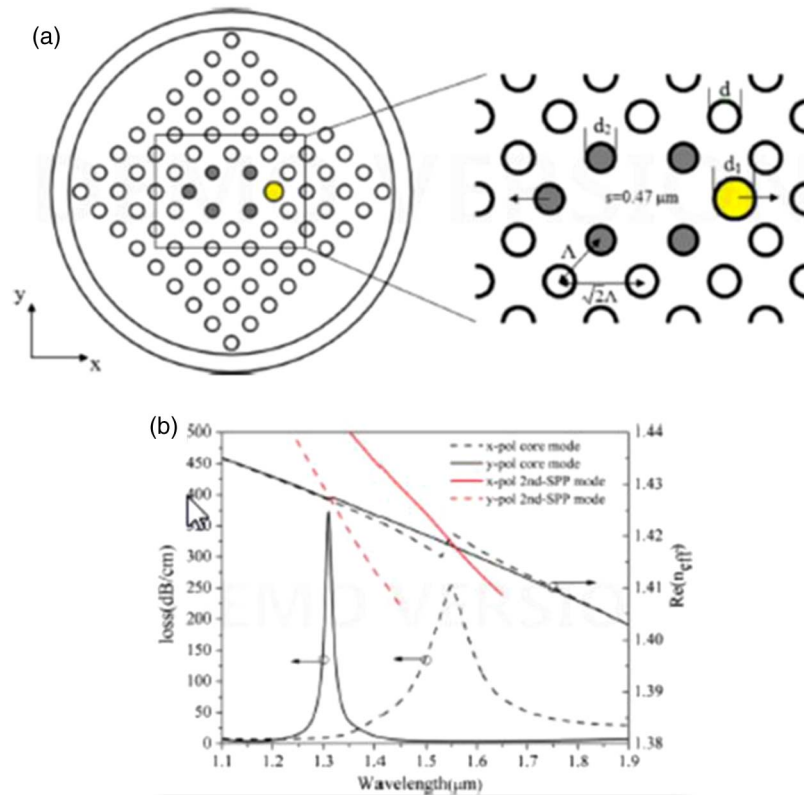
(a) Cross section of the proposed single polarization PCF wavelength splitter. (b) Wavelength dependence of modal losses and the real parts of the effective indices of the *x*- and *y*-polarized core modes. The red lines represent the dispersion relations of the *x*- and *y*-polarized second-order SPP modes. Reprinted with permission from Jiang *et al.*, Opt. Quantum Electron. **48**, 409 (2016) (Figs. 1 and 3) [165]. Copyright © 2016, Springer Science+Business Media New York.

Table 6. Simulated Performance Figures of Metal-Wire-Based Plasmonic PCF Polarization Splitters

PCF Characteristics	Metal Wire	x-pol: Loss (dB/cm)	y-pol: Loss (dB/cm)	Wavelength (nm)	References
PM-solid core PCF with triangular lattice of air holes	Design 1. Au	—	~400	1125	Du 2012 [156]
		~275	—	1275	
	Design 2. Au	—	~40	1295	
		~60	—	1550	
D-shaped PCF with PM triangular lattice	Au	4.0	208.4	1310	Fan 2014 [157]
		4.6	249.5	1550	
SCPCF with triangular lattice	Design 1. Single Au wire	147.48	348.55	1520	Yogalakshmi 2016 [158]
		302	140	1560	
	Design 2. Two separate Au wires	—	451.16	1520	
		352.84	—	1560	
	Design 3. Two adjacent Au wires	187.67	—	1400	
	Design 4. Au coating	<18.52	406.34	1640	
SCPCF with triangular lattice	Two Ag/Au alloy wires	24.42	309.14	~1100	Shi 2014 [159]
SCPCF with triangular lattice and first layer filled with liquid crystal	Au	0.81	446	1550	Chen 2015 [160]
LCPCF with triangular lattice	Au	600	0.0075	1300	Hameed 2015 [161]
		0.092	157.71		
LCPCF with triangular lattice	Two Au wires	443.36	2.24	1310	Liu 2016 [162]
		309.35	6.17	1490	
		258.34	7.86	1550	
Solid core with square lattice	Two Au wires	279.1	—	1020	Zhang 2014 [163]
		399.18	—	1550	
Solid core with square lattice	Two Au wires	231.6	—	1310	An 2016 [164]
		—	237.9	1550	
Solid core with square lattice	Single Au wire	9.41	373.9	1310	Jiang 2016 [165]
		214.31	3.88	1550	
Liquid-crystal-filled core with square lattice	Single Au wire	>248.95	<0.21	1250–2100	Jiang 2016 [166]
		433.25	0.0064	1300	
Spiral PCF with elliptic core	Design 1. Single Au wire	80.14	—	950	Heikal 2015 [167]
		—	63.23	1183	
	Design 2. Multiple Au wire, e.g., 2	94.1	—	980	
		—	56.42	1400	

the two orthogonal polarization states of 2 or ½. The bandwidth of polarization splitting with extinction ratios below −20 dB was over a 146 nm wavelength range for both polarizations [170]. Sun *et al.* improved the design to achieve a shorter device length and broader bandwidth of polarization splitting [171]. Khaleque *et al.* investigated highly birefringent PCF structures with two gold wires embedded in the cladding for ultra-broadband polarization splitters [172,173]. An elliptical metal wire was used in the center of a dual core PCF structure for polarization splitting at 1310 and 1550 nm. The mode couplings occurred for the core guided modes and higher order, i.e., fourth or fifth SPR modes [174]. A broadband polarization splitting device with extinction ratios below −20 dB over a 400 nm wavelength range was demonstrated by Liu *et al.* [175]. A dual core PCF with cladding air holes in a square lattice and a gold wire in the center was designed as an ultra-broadband polarization splitter with an extinction ratio of −78.2 dB at 1550 nm and bandwidth of 430 nm for an extinction ratio better than −20 dB [176]. The performance figures of the polarization splitters using dual core PCF structures containing metal wires are summarized in Table 7.

Besides polarization splitting devices, a dual core PCF with a gold wire in the fiber center region and infiltration of NLC of type E7 in the cladding air holes was designed and demonstrated as a polarization-independent wavelength multiplexer and demultiplexer. The two polarized states at 1550 and 1300 nm can be separated [177]. A square lattice PCF with two defects, i.e., a smaller air hole in the first layer and a gold wire in

Table 7. Performance Figures of Dual Core Metal-Wire-Based Plasmonic PCFs for Polarization Splitters

PCF characteristics metal wire	Length (mm)	ER_x (dB)	ER_y (dB)	Wavelength (nm)	Range (nm) (<-20 dB)	References
			Dual core triangular lattice PCF			
Ag	—	−30.54	—	1550	—	Zhang 2012 [168]
Au	0.5942	~−40	~−40	1310	—	Li 2013 [169]
Ag	63	−39.4	−35.2	1550	x-pol: 1441–1587	Sun 2013 [170]
					y-pol: 1430–1605	
Ag	0.5775	−34	−42	1596	x-pol: 1439–1689	Sun 2015 [171]
					y-pol: 1421–1700	
Au	0.2546	−111	—	1550	x-pol:1420–1980	Khaleque 2015 [172]
Au	0.117	−100	—	1550	x-pol: 1250–1710	Khaleque 2015 [173]
Au	0.585	−50	—	1320	1270–1670	Liu 2015 [175]
		Dual core triangular lattice PCF with elliptical metal wire in the core center				
Au	2.937	−70	—	1310	x-pol:	Fan 2016 [174]
	0.827	−70		1550	~1290–1380	
					~1475–1575	
Ag	3.066	−54	—	1310	x-pol:	
	0.809	−66		1550	~1300–1366	
					~1480–1570	
			Dual core PCF with square lattice			
Au	4.036	−78.2	—	1550	1250–1680	Jiang 2015 [176]

the second layer of the holey cladding, was proposed as a polarization rotator. The design acted as a dual core plasmonic PCF, containing a silica core and a gold wire core that support hybrid supermodes. Simulation results showed that an optimized structure could offer almost 100% polarization conversion ratio at 1550 nm [178].

4.4b. Metal-Film-Coated PCFs and NP-Coated PCFs
Compared with metal-wire-filled PCFs, metal-coated PCFs use less metal and exhibit stronger resonance strength. Therefore, considerable effort has been spent in developing metal-coated PCFs for polarization splitter applications for communication wavelengths. For polarization-dependent devices, high birefringence in PCFs has been obtained by several techniques, such as introducing the asymmetry of cladding or modifying the air holes in size or liquid infiltration in the cladding. Dou *et al.* designed a PCF with a rhombic lattice and different lattice pitch the along *x*- and *y*- directions for achieving high birefringence, as well as two gold-coated air holes in the cladding. By tuning the gold layer thickness, the fiber core mode was coupled to the second-order SPP in the *y*-polarization state at resonance wavelength 1550 nm with confinement loss of 630.2 dB/cm, whereas that of the *x*-polarization state was 36.9 dB/cm. A short device length, such as 2 mm, was sufficient to split the polarizations with ER of −118.7 dB [179]. A PCF with a round lattice was explored for polarization splitter application, showing up to 364.8 dB/cm confinement loss in the *y*-polarization direction at 1550 nm wavelength [180]. Solid-core PCFs with triangular lattices and gold-coated holes have been proposed for polarization splitting devices, with modifications of one or two gold-coated air holes [181,182] or liquid-filled holes in the cladding [183]. Utilizing the high thermo-optic coefficient of a filling liquid such as glycerin, Wang *et al.* demonstrated a design for both temperature sensing and polarization splitting [184].

FWHM of the loss curve can be controlled by varying PCF structural parameters or filling liquids, via which a broadband polarization filter can be designed [185–188]. Liu *et al.* realized a broadband polarization filter from 1.25 to 2 µm with ER smaller than −20 dB with a 1 mm fiber length. The flexibility of controlling the resonance wavelength was also demonstrated by varying gold layer thickness or gold wire

diameters in the report [185]. Wang *et al.* designed a broadband polarization filter based on a PCF with a big gold-coated hole in the holey cladding. A few other air holes in the cladding were modified in diameter to induce high birefringence and facilitate mode coupling between fiber core mode and the SPP mode. The design was shown to exhibit ER lower than −20 dB from 1.26 to 2 µm for a device length greater than 0.21 mm [186]. Han *et al.* reported a highly birefringent PCF-based single polarization single-mode fiber with two gold-coated holes filled with liquid in the cladding for broadband polarization splitting [187]. Chen *et al.* reported a D-shaped PM PCF with two big holes next to the solid core and gold coated on the surface for polarization splitter application. A cross section of the proposed fiber is shown in Fig. 22(c). Mode coupling between the fiber core mode and different higher order SPR modes in *y*-polarized states resulted in different phase-matching wavelengths. Particularly for the seventh-order SPR mode, the resonance wavelength was 1560 nm. The phase-matching plots and corresponding confinement loss of the core mode are shown in Figs. 22(a) and 22(b). Considering a 4 mm fiber device, an ultra-broadband polarization splitter exceeding 1 µm with ER < −20 dB was achieved, as shown in Fig. 22(d) [188].

Chen *et al.* reported a gold-film-coated D-shaped PCF polarization splitter, and the bandwidths were 40 and 60 nm for *x*- and *y*- polarization modes with ER better than −20 dB [189]. Fan *et al.* compared the polarization splitting between a dual core PCF with a gold wire in the center and a dual core PCF with a gold-film-coated hole in the center, and found that due to stronger resonance coupling in a gold-film-coated PCF, the bandwidth could reach 220 nm with ER better than −20 dB for a device length of 0.542 mm [190].

Square lattices have shown flexibility in controlling the birefringent properties that are desirable for polarization splitters. PCFs with one or more gold-coated holes in a square lattice cladding have been proposed for a polarization splitter at 1310 and

Figure 22
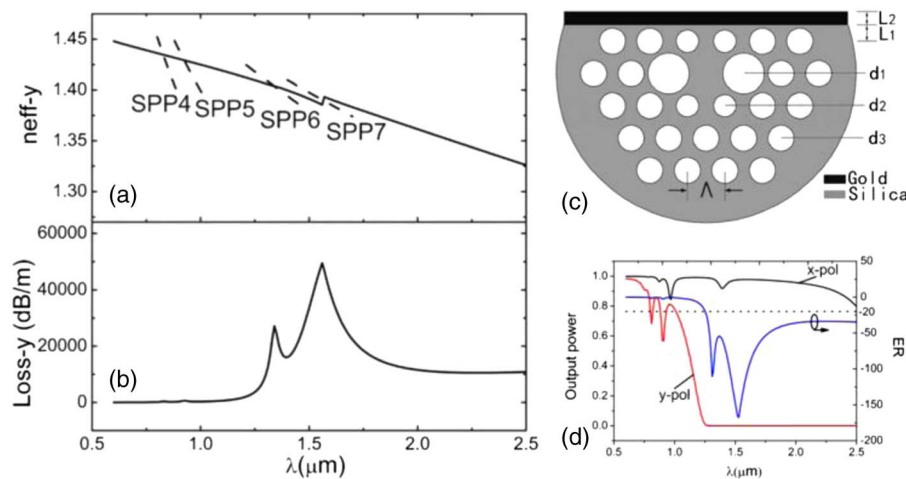
(a) Effective refractive indices of core modes and SPP modes in the *y*-polarization direction. (b) Confinement loss spectra of core modes in the *y*-polarization direction. (c) The schematic of the d-shaped PCF polarization splitter. The gold film is deposited on the polished plane. (d) The output power and ER as the thickness of gold film increasing to 0.05 µm. The transferring length is set as 4 mm. Reprinted from Chen *et al.*, Plasmonics **10**, 1239–1242 (2015) (Figs. 1, 4, and 6) [188]. Copyright © 2015, Springer Science+Business Media New York.

Table 8. Performance of Gold-Coated PCF-Based Polarization Splitters

Au-Coated PCF Characteristics	x-pol: Loss[a] (dB/cm)	y-pol: Loss (dB/cm)	Wavelength (nm)	Range (nm) (<−20 dB)	References
Solid core with rhombic lattice					
—	630.2	36.9	1550	—	Dou 2015 [179]
PM-SCPCF with round lattice					
PM	~25	364.8	1550	130(0.8 mm)	Hao 2016 [180]
Solid core with triangular lattice					
A big gold-coated air hole	—	1362.53	1310	—	Wang 2016 [181]
		1676.07	1550		
Liquid filled	~20	508.6	1311	—	Xue 2013 [183]
Liquid core, two coated holes in the cladding	2.02	412.91	1310	—	Jiang 2015 [182]
	5.29	536.25	1550		
One hole filled with glycerin	~100	445.958	1400	—	Wang 2016 [184]
	321.442	~100	1480		
Au with different thickness	~20	377.19	1310	1250–2000	Liu 2015 [185]
	~10	417.21	1480	(loss in y-	
	~10	418.02	1550	>350 dB/cm)	
Modified triangular lattice and a big gold-coated air hole	857.8	—	1310	1260–2000 (>0.21 mm)	Wang 2016 [186]
Two holes filled with liquid	—	~250	~1450	1350–1700 (30 dB/cm)	Han 2015 [187]
D-shaped	~0.5	495.21	1560	1250–2500 (4 mm)	Chen 2015 [188]
Dual core PCF with triangular lattice					
D-shaped	-	-	1550	1530–1570 (0.782 mm)	Chen 2015 [189]
Coated hole in the center between dual core	384.6	444.1	1260	1380–1600 (0.542 mm)	Fan 2015 [190]
Solid core with square lattice					
PMPCF with four elliptical holes next to the core and two coated holes in the cladding	102.6	3.5	1310	—	Chen 2014 [191]
	1.7	245	1550		
One coated hole in the cladding	123.46	—	1310	—	Liu 2015 [192]
	—	410.04	1550		
Solid core with square lattice rotated by 45 °C					
Two coated holes in the cladding	~20	720	1310	1200–2000 (>0.2 mm)	Wang 2015 [193]
Design 1: one large Au-coated hole	—	517	1310		Zi 2015 [194]
		375	1550		
Design 2: two large Au-coated holes on opposite corners	—	701	1310		
Design 3: two large Au-coated holes on orthogonal corner	~10	475	1310	181	Zi 2015 [195]
	369	~20	1550	423 (1 mm)	
Two coated holes in the cladding	—	452.4	1310	430	Liu 2015 [196]
	—	102	1550	(3 mm)	
Squeezed square	1221	1.6	1310	—	Khaleque 2015 [197]
Two Au-coated holes, modified squeezed square lattice	771.5	2.7	1310	—	Li 2015 [198]
Metal NPs					
PMPCF, the two large holes filled by NPs and PDMS	1200	119	442	—	Poudereux 2015 [199]

[a]Some of the values are not explicitly stated in the paper; we report an estimated value based on the graph presented in the work. The field is left empty if such information is not available from the paper.

1550 nm [191,192]. Chen *et al.* investigated a PCF with a solid core formed from three "missing" air holes in a square lattice holey structure. The core was surrounded by two gold-film-coated holes and four large elliptical holes in the first layer. Polarization-dependent coupling between the fiber core mode and the SPP mode resulted in desirable polarization splitter performance at communication wavelengths [191]. Another PCF design with one gold-film-coated hole and a few other holes modified

in diameter in the square lattice was shown to improve the polarization splitting at communication wavelengths, e.g., 1310 and 1550 nm and short device length [192]. There have been reports on PCFs with a square lattice rotated by 45° [193–196] and a squeezed lattice rotated by 45° [197,198]. Wang *et al.* reported a PCF design with two coated holes in the cladding and demonstrated bandwidth of 800 nm for ER better than −20 dB for a fiber length longer than 0.2 mm [193]. Zi *et al.* designed a PCF with a squeezed square lattice and two large gold-coated holes on the orthogonal corner, and demonstrated bandwidths of 181 and 423 nm for wavelength windows of 1310 and 1550 nm, respectively [195]. Liu *et al.* demonstrated an optimized design to achieve high confinement loss of the *y*-polarized core mode at 1310 and 1550 nm, up to 452.4 and 102 dB/m, respectively. A 3 mm length device would be able to achieve more than 430 nm bandwidth of ER better than −20 dB [196].

In addition to using metal wires and metal films, metal NPs have also been proposed in designs for LSPR-based polarization filters. Poudereux *et al.* selected a PM-PCF structure filled with a mixture of Ag NPs in a matrix of polydimethylsiloxane (PDMS), showing attenuation up to 1200 dB/cm in the *x*-polarization direction and 119 dB/cm in the *y*-polarization direction at a LSPR resonance wavelength around 442 nm. Tuning of the LSPR resonance was also demonstrated through NP size for attenuation amplitude and through temperature for resonance wavelength [199]. Table 8 summarizes the performance of polarization splitters based on gold-coated PCFs. The presented designs usually possess high loss of a few hundred dB/cm for one polarization, with much lower loss for the orthogonal polarization for effective polarization splitting within a very short device length, e.g., sub-millimeter to millimeter scale, which is a challenging task for fabrication. A plasmonic fiber device for polarization filtering and splitting should also be developed as an integrated photonics element rather than a fiber due to their high loss.

4.5. Others

Unlike pure silica glass in which the nonlinear coefficient is a real number and almost constant, composite materials such as gold–silver NPs have complex nonlinear coefficients. The inclusion of composite materials in PCFs leads to unusual nonlinear properties, which is favorable for the study of ultrashort pulses and soliton dynamics [200]. Metal-coated silicon nanowire embedded plasmonic PCFs have been shown to support efficient propagation of SPP modes in the nanowire and to have a high threshold power for undesirable free carrier effects, showing potential in Kerr-related nonlinear applications with relative high power [201]. Different from utilizing the plasmonic effects, PCFs with metal nanowire arrays surrounded by a dielectric have been proposed for electromagnetic invisibility. Such metamaterial-based fibers possess a RI that can be matched to the surroundings [202].

5. CONCLUSION

Over the past several years, there has been substantial growth in the design, fabrication, and application development of plasmonic PCF devices. The idea is to build a novel class of plasmonic components with enhanced interaction between light and medium, by integrating the capabilities of plasmonics in a robust and flexible PCF platform for sensing and communication applications.

First, substantial development has been made in the fabrication of plasmonic PCFs. Various technologies have been developed for fabrication of metal-nanowire-filled PCFs, such as a modified stack-and-draw technique [42], a high-pressure microfluidic chemical deposition technique [44], a high-temperature pressure cell technique

[45,46], a pressure-assisted splicing technique [47], and the capillary effect of filling nanowires in a liquid mixture [56,57]. Metal-coated PCFs have been reported with fabrication techniques including high-pressure microfluidic chemical deposition [58], the silver mirror reaction for suspended core PCFs [59], the two-stage draw technique for polymer PCFs [60], electroless plating [61], sputtering [62], and thermal evaporation for tapered PCFs [67]. NP-coated PCFs can be realized by techniques based on capillary effects [68], or assisted by high-pressure injection [81,82], low-pressure chemical deposition using a combination of self-assembly and microfluidics [85] [86], high-pressure chemical deposition [87], and stack-and-draw [89]. Continuing efforts in improving and maturation of fabrication techniques is essential to advance the field and will drive realization and advancement of plasmonic PCF devices and components with better quality, more robustness, and higher reliability.

Second, a diversity of plasmonic PCF designs has flourished in recent years, as can be seen from the wide range of device schemes specifically tailored for many applications, including RI sensing and biosensing, multi-analyte sensing, temperature sensing, dual parameter sensing, and polarization splitting. Rapid updates have been reported in the benchmarking of device performance, such as sensor sensitivity, polarization splitting extinction ratio, and bandwidth. These efforts have provided a solid foundation for theoretical and experimental investigations, as well as guidance for future device development.

The realization of plasmonic PCF structures with intricate designs and features is limited due to the metal structures achievable in fabrication. First, it is difficult to achieve small diameters and high aspect ratio wires in PCFs. Most fabrication methods reported so far produce micrometer or sub-micrometer size metal wires up to a length scale of centimeters. Second, it remains a challenge for sputtering and evaporation techniques to achieve continuous uniformity of metal coatings inside and outside of the PCFs. Third, better uniformity of metal layers in the PCF was achieved using chemical deposition methods with more complicated conditions, e.g., high pressure or high temperature. In addition, different fiber materials and structures require different fabrication techniques. For instance, polymer fibers have much lower drawing temperatures compared to silica fibers. PCFs with different fiber structures and metal structures, e.g., air hole size, air filling fraction, single or multiple wires, complete or selective coating, and internal or external fabrication of metal structures in the PCF, all contribute to different requirements or procedures in fabrication. Last, the proposed designs of plasmonic fiber devices, e.g., sensors and polarization splitters, are showing extremely high losses associated with very short device lengths of sub-millimeters. However, realization of such plasmonic fiber devices as in-fiber devices would require more flexibility in the device length to millimeters or centimeters for practical development. All of the considerations discussed herein should be taken into account in the design process to ensure good feasibility of the plasmonic PCF structure.

It is encouraging to see the vast possibilities in different designs of metallic PCF structures with desirable characteristics in numerous reports. Continuous development in fabrication technologies is the fundamental enabler to realizing plasmonic PCF structures and devices with promised functionalities and performance, which is also the key to driving development of practical applications based on plasmonic PCF devices.

> Although as thin as human hairs, optical fibers have revolutionized our life in many ways. It is exciting to use optical fibers to manipulate light and create solutions to address real-life problems.

REFERENCES

1. J. Homola, "Surface plasmon resonance sensors for detection of chemical and biological species," Chem. Rev. **108**, 462–493 (2008).
2. W. L. Barnes, A. Dereux, and T. W. Ebbesen, "Surface plasmon subwavelength optics," Nature **424**, 824–830 (2003).
3. R. C. Jorgenson and S. S. Yee, "A fiber-optic chemical sensor based on surface plasmon resonance," Sens. Actuators B Chem. **12**, 213–220 (1993).
4. R. Slavík, J. Homola, and J. Čtyroký, "Single-mode optical fiber surface plasmon resonance sensor," Sens. Actuators B Chem. **54**, 74–79 (1999).
5. W.-H. Lin, Y.-C. Tsai, Y.-C. Tsao, and J.-K. Tai, "An enhanced optical multimode fiber sensor based on surface plasmon resonance with cascaded structure," IEEE Photon. Technol. Lett. **20**, 1287–1289 (2008).
6. A. Trouillet, C. Ronot-Trioli, C. Veillas, and H. Gagnaire, "Chemical sensing by surface plasmon resonance in a multimode optical fibre," Pure Appl. Opt. **5**, 227–237 (1996).
7. B.-H. Liu, Y.-X. Jiang, X.-S. Zhu, X.-L. Tang, and Y.-W. Shi, "Hollow fiber surface plasmon resonance sensor for the detection of liquid with high refractive index," Opt. Express **21**, 32349–32357 (2013).
8. R. J. Whelan and R. N. Zare, "Surface plasmon resonance detection for capillary electrophoresis separations," Anal. Chem. **75**, 1542–1547 (2003).
9. R. Jha, R. K. Verma, and B. D. Gupta, "Surface plasmon resonance-based tapered fiber optic sensor: sensitivity enhancement by introducing a Teflon layer between core and metal layer," Plasmonics **3**, 151–156 (2008).
10. Y.-C. Kim, W. Peng, S. Banerji, and K. Booksh, "Tapered fiber optic surface plasmon resonance sensor for analyses of vapor and liquid phases," Opt. Lett. **30**, 2218–2220 (2005).
11. H.-Y. Lin, C.-H. Huang, G.-L. Cheng, N.-K. Chen, and H.-C. Chui, "Tapered optical fiber sensor based on localized surface plasmon resonance," Opt. Express **20**, 21693–21701 (2012).
12. S. K. Srivastava, V. Arora, S. Sapra, and B. D. Gupta, "Localized surface plasmon resonance-based fiber optic U-shaped biosensor for the detection of blood glucose," Plasmonics **7**, 261–268 (2012).
13. R. K. Verma and B. D. Gupta, "Theoretical modelling of a bi-dimensional U-shaped surface plasmon resonance based fibre optic sensor for sensitivity enhancement," J. Phys. D **41**, 095106 (2008).
14. A. Patnaik, K. Senthilnathan, and R. Jha, "Graphene-based conducting metal oxide coated D-shaped optical fiber SPR sensor," IEEE Photon. Technol. Lett. **27**, 2437–2440 (2015).
15. N. Rezaei and A. Yahaghi, "A high sensitivity surface plasmon resonance D-shaped fiber sensor based on a waveguide-coupled bimetallic structure: modeling and optimization," IEEE Sens. J. **14**, 3611–3615 (2014).
16. H.-Y. Lin, W.-H. Tsai, Y.-C. Tsao, and B.-C. Sheu, "Side-polished multimode fiber biosensor based on surface plasmon resonance with halogen light," Appl. Opt. **46**, 800–806 (2007).

17. H.-Y. Lin, Y.-C. Tsao, W.-H. Tsai, Y.-W. Yang, T.-R. Yan, and B.-C. Sheu, "Development and application of side-polished fiber immunosensor based on surface plasmon resonance for the detection of Legionella pneumophila with halogens light and 850 nm-LED," Sens. Actuators A **138**, 299–305 (2007).

18. T.-J. Lin and C.-T. Lou, "Reflection-based localized surface plasmon resonance fiber-optic probe for chemical and biochemical sensing at high-pressure conditions," J. Supercrit. Fluids **41**, 317–325 (2007).

19. Y. Lin, Y. Zou, and R. G. Lindquist, "A reflection-based localized surface plasmon resonance fiber-optic probe for biochemical sensing," Biomed. Opt. Express **2**, 478–484 (2011).

20. L.-Y. Shao, Y. Shevchenko, and J. Albert, "Intrinsic temperature sensitivity of tilted fiber Bragg grating based surface plasmon resonance sensors," Opt. Express **18**, 11464–11471 (2010).

21. C. Shen, Y. Zhang, W. Zhou, and J. Albert, "Au-coated tilted fiber Bragg grating twist sensor based on surface plasmon resonance," Appl. Phys. Lett. **104**, 071106 (2014).

22. T. Schuster, R. Herschel, N. Neumann, and C. G. Schäffer, "Miniaturized long-period fiber grating assisted surface plasmon resonance sensor," J. Lightwave Technol. **30**, 1003–1008 (2012).

23. Y. J. He, "Investigation of LPG-SPR sensors using the finite element method and eigenmode expansion method," Opt. Express **21**, 13875–13895 (2013).

24. J. C. Knight, "Photonic crystal fibres," Nature **424**, 847–851 (2003).

25. P. Russell, "Photonic crystal fibers," Science **299**, 358–362 (2003).

26. J. Villatoro and J. Zubia, "New perspectives in photonic crystal fibre sensors," Opt. Laser Technol. **78**, 67–75 (2016).

27. Y. Zhao, Z. Deng, and J. Li, "Photonic crystal fiber based surface plasmon resonance chemical sensors," Sens. Actuators B **202**, 557–567 (2014).

28. B. D. Gupta and R. K. Verma, "Surface plasmon resonance-based fiber optic sensors: principle, probe designs, and some applications," J. Sens. **2009**, 1–12 (2009).

29. A. K. Sharma, R. Jha, and B. D. Gupta, "Fiber-optic sensors based on surface plasmon resonance: a comprehensive review," IEEE Sens. J. **7**, 1118–1129 (2007).

30. X. Yang, C. Gu, F. Qian, Y. Li, and J. Z. Zhang, "Highly sensitive detection of proteins and bacteria in aqueous solution using surface-enhanced Raman scattering and optical fibers," Anal. Chem. **83**, 5888–5894 (2011).

31. A. Urrutia, J. Goicoechea, and F. J. Arregui, "Optical fiber sensors based on nanoparticle-embedded coatings," J. Sens. **2015**, 1–18 (2015).

32. C. Caucheteur, T. Guo, and J. Albert, "Review of plasmonic fiber optic biochemical sensors: improving the limit of detection," Anal. Bioanal. Chem. **407**, 3883–3897 (2015).

33. E. Kretschmann and H. Z. Raether, "Radiative decay of non radiative surface plasmons excited by light," Z. Naturforsch. A **23**, 2135–2136 (1968).

34. M.-H. Chiu, C.-H. Shih, and M.-H. Chi, "Optimum sensitivity of single-mode D-type optical fiber sensor in the intensity measurement," Sens. Actuators B **123**, 1120–1124 (2007).

35. L. Coelho, J. M. M. M. de Almeida, J. L. Santos, R. A. S. Ferreira, P. S. André, and D. Viegas, "Sensing structure based on surface plasmon resonance in chemically etched single mode optical fibres," Plasmonics **10**, 319–327 (2015).

36. M. Born and E. Wolf, "Basic properties of the electromagnetic field," in *Principles of Optics*, 7th ed. (Cambridge University, 1999), pp. 752–758.

37. P. Yeh, *Optical Waves in Layered Media* (Wiley, 1998).

38. A. Nagasaki, K. Saitoh, and M. Koshiba, "Polarization characteristics of photonic crystal fibers selectively filled with metal wires into cladding air holes," Opt. Express **19**, 3799–3808 (2011).

39. J. N. Dash and R. Jha, "SPR biosensor based on polymer PCF coated with conducting metal oxide," IEEE Photon. Technol. Lett. **26**, 594–598 (2014).

40. C. Sauvan, J. P. Hugonin, I. S. Maksymov, and P. Lalanne, "Theory of the spontaneous optical emission of nanosize photonic and plasmonic resonators," Phys. Rev. Lett. **110**, 237401 (2013).

41. M. Sun, Y. Wang, Z. N. Chen, Y. Gong, J. Lim, and X. Qing, "Nanostars on a fiber facet with near field enhancement for surface-enhanced Raman scattering detection," Appl. Phys. A **115**, 87–91 (2014).

42. J. Hou, D. Bird, A. George, S. Maier, B. T. Kuhlmey, and J. C. Knight, "Metallic mode confinement in microstructured fibres," Opt. Express **16**, 5983–5990 (2008).

43. A. Tuniz, B. T. Kuhlmey, R. Lwin, A. Wang, J. Anthony, R. Leonhardt, and S. C. Fleming, "Drawn metamaterials with plasmonic response at terahertz frequencies," Appl. Phys. Lett. **96**, 191101 (2010).

44. C. E. Finlayson, A. Amezcua-Correa, and P. J. A. Sazio, "Electrical and Raman characterization of silicon and germanium-filled microstructured optical fibers," Appl. Phys. Lett. **90**, 132110 (2007).

45. M. A. Schmidt, L. N. P. Sempere, H. K. Tyagi, C. G. Poulton, and P. St.J. Russell, "Waveguiding and plasmon resonances in two-dimensional photonic lattices of gold and silver nanowires," Phys. Rev. B **77**, 033417 (2008).

46. H. W. Lee, M. A. Schmidt, H. K. Tyagi, L. P. Sempere, and P. St.J. Russell, "Polarization-dependent coupling to plasmon modes on submicron gold wire in photonic crystal fiber," Appl. Phys. Lett. **93**, 111102 (2008).

47. H. W. Lee, M. A. Schmidt, R. F. Russel, N. Y. Joly, H. K. Tyagi, P. Uebel, and P. St.J. Russell, "Pressure-assisted melt-filling and optical characterization of Au nano-wires in microstructured fibers," Opt. Express **19**, 12180–12189 (2011).

48. I. W. Donald and B. L. Metcalfe, "The preparation, properties and applications of some glass-coated metal filaments prepared by the Taylor-wire process," J. Mater. Sci. **31**, 1139–1149 (1996).

49. X. Zhang, Z. Ma, Z.-Y. Yuan, and M. Su, "Mass-productions of vertically aligned extremely long metallic micro/nanowires using fiber drawing nanomanufacturing," Adv. Mater. **20**, 1310–1314 (2008).

50. M. Yaman, T. Khudiyev, E. Ozgur, M. Kanik, O. Aktas, E. O. Ozgur, H. Deniz, E. Korkut, and M. Bayindir, "Arrays of indefinitely long uniform nanowires and nanotubes," Nat. Mater. **10**, 494–501 (2011).

51. H. Tyagi, H. W. Lee, P. Uebel, M. A. Schmidt, N. Joly, M. Scharrer, and P. St.J. Russell, "Plasmon resonances on gold nanowires directly," Opt. Lett. **35**, 2573–2575 (2010).

52. A. Witkowska, K. Lai, S. G. Leon-Saval, W. J. Wadsworth, and T. A. Birks, "All-fiber anamorphic core-shape transitions," Opt. Lett. **31**, 2672–2674 (2006).

53. P. Uebel, M. A. Schmidt, H. W. Lee, and P. St.J. Russell, "Polarisation-resolved near-field mapping of a coupled gold nanowire array," Opt. Express **20**, 28409–28417 (2012).

54. H. W. Lee, M. A. Schmidt, and P. St.J. Russell, "Excitation of a nanowire 'molecule' in gold-filled photonic crystal fiber," Opt. Lett. **37**, 2946–2948 (2012).

55. C. Jain, A. Tuniz, K. Reuther, T. Wieduwilt, M. Rettenmayr, and M. A. Schmidt, "Micron-sized gold-nickel alloy wire integrated silica optical fibers," Opt. Express **6**, 1790–1799 (2016).

56. Y. Lu, M. T. Wang, C. J. Hao, Z. Q. Zhao, and J. Q. Yao, "Temperature sensing using photonic crystal fiber filled with silver nanowires and liquid," IEEE Photon. J. **6**, 680137 (2014).

57. X. C. Yang, Y. Lu, B. L. Liu, and J. Q. Yao, "Temperature sensor based on photonic crystal fiber filled with liquid and silver nanowires," IEEE Photon. J. **8**, 6803309 (2016).

58. P. J. A. Sazio, A. Amezcua-Correa, C. E. Finlayson, J. R. Hayes, T. J. Scheidemantel, N. F. Baril, B. R. Jackson, D. J. Won, F. Zhang, E. R. Margine, V. Gopolan, V. H. Crespi, and J. V. Badding, "Microstructured optical fibers as high-pressure microfluidic reactors," Science **311**, 1583–1586 (2006).

59. J. Boehm, A. Francois, H. Ebendorff-Heidepriem, and T. M. Monro, "Chemical deposition of silver for the fabrication of surface plasmon microstructured optical fibre sensors," Plasmonics **6**, 133–136 (2011).

60. X. Zhang, R. Wang, F. M. Cox, B. T. Kuhlmey, and M. C. J. Large, "Selective coating of holes in microstructured optical fiber and its application to in-fiber absorptive polarizers," Opt. Express **15**, 16270–16278 (2007).

61. E. Klantsataya, A. Francois, H. Ebendorff-Heidepriem, P. Hoffmann, and T. M. Monro, "Surface plasmon scattering in exposed core optical fiber for enhanced resolution refractive index sensing," Sensors **15**, 25090–25102 (2015).

62. A. Wang, A. Docherty, B. T. Kuhlmey, F. M. Cox, and M. C. J. Large, "Side-hole fiber sensor based on surface plasmon resonance," Opt. Lett. **34**, 3890–3892 (2009).

63. X. Yu, D. Yong, H. Zhang, H. Li, Y. Zhang, C. C. Chan, H.-P. Ho, H. Liu, and D. Liu, "Plasmonic enhanced fluorescence spectroscopy using side-polished microstructured optical fiber," Sens. Actuators B **160**, 196–201 (2011).

64. D. J. J. Hu, J. L. Lim, M. K. Park, L. T. H. Kao, Y. Wang, H. Wei, and W. Tong, "Photonic crystal fiber-based interferometric biosensor for streptavidin and biotin detection," IEEE J. Sel. Top. Quantum Electron. **18**, 1293–1297 (2012).

65. D. J. J. Hu, J. L. Lim, M. Jiang, Y. Wang, F. Luan, P. P. Shum, H. Wei, and W. Tong, "Long period grating cascaded to photonic crystal fiber modal interferometer for simultaneous measurement of temperature and refractive index," Opt. Lett. **37**, 2283–2285 (2012).

66. W. C. Wong, C. C. Chan, J. L. Boo, Z. Y. Teo, Z. Q. Tou, H. B. Yang, C. M. Li, and K. C. Leong, "Photonic crystal fiber surface plasmon resonance biosensor based on protein G immobilization," IEEE J. Sel. Top. Quantum Electron. **19**, 460217 (2013).

67. H. E. Arabi, M. Pournoury, J. H. Park, S. Im, and K. Oh, "Plasmonically enhanced optical transmission through a metalized nanostructured photonic crystal fiber taper," Opt. Lett. **36**, 2029–2031 (2011).

68. T. K. Sau and C. J. Murphy, "Self-assembly patterns formed upon solvent evaporation of aqueous cetyltrimethylammonium bromide-coated gold nanoparticles of various shapes," Langmuir **21**, 2923–2929 (2005).

69. H. Yan, J. Liu, C. Yang, G. Jin, C. Gu, and L. Hou, "Novel index-guided photonic crystal fiber surface-enhanced Raman scattering probe," Opt. Express **16**, 8300–8305 (2008).

70. Z. Xie, Y. Lu, H. Wei, J. Yan, P. Wang, and H. Ming, "Broad spectral photonic crystal fiber surface enhanced Raman scattering probe," Appl. Phys. B **95**, 751–755 (2009).

71. N. Zhang, G. Humbert, T. Gong, P. P. Shum, K. Li, J.-L. Auguste, Z. Wu, D. J. J. Hu, F. Luan, Q. X. Dinh, M. Olivo, and L. Wei, "Side-channel photonic crystal fiber for surface enhanced Raman scattering sensing," Sens. Actuators B **223**, 195–201 (2016).

72. H. Yan, C. Gu, C. Yang, J. Liu, G. Jin, J. Zhao, L. Hou, and Y. Yao, "Hollow core photonic crystal fiber surface-enhanced Raman probe," Appl. Phys. Lett. **89**, 204101 (2006).

73. F. M. Cox, A. Argyros, M. C. J. Large, and S. Kalluri, "Surface enhanced Raman scattering in a hollow core microstructured optical fiber," Opt. Express **15**, 13675–13681 (2007).

74. Y. Han, S. Tan, M. K. K. Oo, D. Pristinski, S. Sukhishvili, and H. Du, "Towards full-length accumulative surface-enhanced Raman scattering-active photonic crystal fibers," Adv. Mater. **22**, 2647–2651 (2010).

75. V. S. Tiwari, A. Khetani, A. Momenpour, and H. Anis, "Optimum size and volume of nanoparticle within hollow core photonic crystal fiber," IEEE J. Sel. Top. Quantum Electron. **20**, 7300608 (2014).

76. Y. Zhang, C. Shi, C. Gu, L. Seballos, and J. Z. Zhang, "Liquid core photonic crystal fiber sensor based on surface enhanced Raman scattering," Appl. Phys. Lett. **90**, 193504 (2007).

77. J. Irizar, J. Dinglasan, J. B. Goh, A. Khetani, H. Anis, D. Anderson, C. Goh, and A. S. Helmy, "Raman spectroscopy of nanoparticles using hollow-core photonic crystal fibers," IEEE J. Sel. Top. Quantum Electron. **14**, 1214–1222 (2008).

78. X. Yang, C. Shi, D. Wheeler, R. Newhouse, B. Chen, J. Z. Zhang, and C. Gu, "High-sensitivity molecular sensing using hollow-core photonic crystal fiber and surface-enhanced Raman scattering," J. Opt. Soc. Am. A **27**, 977–984 (2010).

79. C. Shi, C. Lu, C. Gu, L. Tian, R. Newhouse, S. Chen, and J. Z. Zhang, "Inner wall coated hollow core waveguide sensor based on double substrate surface enhanced Raman scattering," Appl. Phys. Lett. **93**, 153101 (2008).

80. X. Yang, C. Shi, R. Newhouse, J. Z. Zhang, and C. Gu, "Hollow-core photonic crystal fibers for surface-enhanced Raman scattering probes," Int. J. Opt. **2011**, 751610 (2010).

81. M. K. K. Oo, Y. Han, J. Kanka, S. Sukhishvili, and H. Du, "Structure fits the purpose: photonic crystal fibers for evanescent field surface enhanced Raman spectroscopy," Opt. Lett. **35**, 466–468 (2010).

82. M. K. K. Oo, Y. Han, R. Martini, S. Sukhishvili, and H. Du, "Forward-propagating surface-enhanced Raman scattering and intensity distribution in photonic crystal fiber with immobilized Ag nanoparticles," Opt. Lett. **34**, 968–970 (2009).

83. Y. Zhang, D. Yong, X. Yu, L. Xia, D. Liu, and Y. Zhang, "Amplification of surface-enhance Raman scattering in photonic crystal fiber using offset launch method," Plasmonics **8**, 209–215 (2013).

84. A. Khetani, J. Riordon, V. Tiwari, A. Momenpour, M. Godin, and H. Anis, "Hollow core photonic crystal fiber as a reusable Raman biosensor," Opt. Express **21**, 12340–12350 (2013).

85. A. Csaki, F. Jahn, I. Latka, T. Henkel, D. Malsch, T. Schneider, K. Schroder, K. Schuster, A. Schwuchow, R. Spittel, D. Zopf, and W. Fritzsche, "Nanoparticle layer deposition for plasmonic tuning of microstructured optical fibers," Small **6**, 2584–2589 (2010).

86. K. Schröder, A. Csáki, A. Schwuchow, F. Jahn, K. Strelau, I. Latka, T. Henkel, D. Malsch, K. Schuster, K. Weber, T. Schneider, R. Möller, and W. Fritzsche, "Functionalization of microstructured optical fibers by internal nanoparticle mono-layers for plasmonic biosensor applications," IEEE Sens. J. **12**, 218–224 (2012).

87. A. Amezcua-Correa, J. Yang, C. E. Finlayson, A. C. Peacor, J. Hayes, P. Sazio, J. J. Baumberg, and S. M. Howdle, "Surface-enhanced Raman scattering using microstructured optical fiber substrates," Adv. Funct. Mater. **17**, 2024–2030 (2007).

88. A. C. Peacock, A. Amezcua-Correa, J. Yang, P. J. A. Sazio, and S. M. Howdle, "Highly efficient surface enhanced Raman scattering using microstructured

optical fibers with enhanced plasmonic interactions," Appl. Phys. Lett. **92**, 141113 (2008).

89. L. Bigot, H. E. Hamzaoui, A. L. Rouge, G. Bouwmans, F. Chassagneux, B. Capoen, and M. Bouazaoui, "Linear and nonlinear optical properties of gold nano-particle-doped photonic crystal fiber," Opt. Express **19**, 19061–19066 (2011).

90. U. S. Dinish, C. Y. Fu, K. S. Soh, R. Bhuvaneswari, A. Kumar, and M. Olivo, "Highly sensitive SERS detection of cancer proteins in low sample volume using hollow core photonic crystal fiber," Biosens. Bioelectron. **33**, 293–298 (2012).

91. U. S. Dinish, G. Balasundara, Y. T. Chang, and M. Olivo, "Sensitive multiplex detection of serological liver cancer biomarkers using SERS-active photonic crystal fiber probe," J. Biophoton. **7**, 956–965 (2014).

92. A. Khetani, A. Momenpour, E. I. Alarcon, and H. Anis, "Hollow core photonic crystal fiber for monitoring leukemia cells using surface enhanced Raman scattering (SERS)," Opt. Express **6**, 4599–4609 (2015).

93. T. Gong, Y. Cui, D. Goh, K. K. Voon, P. P. Shum, G. Humbert, J.-L. Auguste, X.-Q. Dinh, K.-T. Yong, and M. Olivo, "Highly sensitive SERS detection and quantification of sialic acid on single cell using photonic-crystal fiber with gold nanoparticles," Biosens. Bioelectron. **64**, 227–233 (2015).

94. P. Pinkhasova, H. Chen, J. Kanka, P. Mergo, and H. Du, "Nanotag-enabled photonic crystal fiber as quantitative surface-enhanced Raman scattering optofluidic platform," Appl. Phys. Lett. **106**, 071106 (2015).

95. A. Hassani and M. Skorobogatiy, "Design of the microstructured optical fiber-based surface plasmon resonance sensors with enhanced microfluidics," Opt. Express **14**, 11616–11621 (2006).

96. A. Hassani and M. Skorobogatiy, "Design criteria for microstructured-optical-fiber-based surface-plasmon-resonance sensors," J. Opt. Soc. Am. B **24**, 1423–1429 (2007).

97. L. Zheng, X. Zhang, X. Ren, J. Gao, L. Shi, X. Liu, Q. Wang, and Y. Huang, "Surface plasmon resonance sensors based on Ag-metalized nanolayer in microstructured optical fibers," Opt. Laser Technol. **43**, 960–964 (2011).

98. X. Yu, Y. Zhang, S. Pan, P. Shum, M. Yan, Y. Leviatan, and C. Li, "A selectively coated photonic crystal fiber based surface plasmon resonance sensor," J. Opt. **12**, 015005 (2010).

99. W. Wei, X. Zhang, X. Guo, L. Zheng, J. Gao, W. Shi, Q. Wang, Y. Huang, and X. Ren, "Refractive index sensors based on Ag-metalized nanolayer in microstructured optical fibers," Optik **123**, 1167–1170 (2012).

100. E. K. Akowuah, T. Gorman, H. Ademgil, S. Haxha, G. K. Robinson, and J. V. Oliver, "Numerical analysis of a photonic crystal fiber for biosensing applications," IEEE J. Quantum Electron. **48**, 1403–1410 (2012).

101. S. I. Azzam, M. F. O. Hameed, R. E. A. Shehata, A. M. Heikal, and S. S. A. Obayya, "Multichannel photonic crystal fiber surface plasmon resonance based sensor," Opt. Quantum Electron. **48**, 142 (2016).

102. Y. Lu, C.-J. Hao, B.-Q. Wu, M. Musideke, L.-C. Duan, W.-Q. Wen, and J.-Q. Yao, "Surface plasmon resonance sensor based on polymer photonic crystal fibers with metal nanolayers," Sensors **13**, 956–965 (2013).

103. R. Otupiri, S. K. Akowuah, S. Haxha, H. Ademgil, F. Abdelmalek, and A. Aggoun, "A novel birefringent photonic crystal fiber surface plasmon resonance biosensor," IEEE Photon. J. **6**, 6801711 (2014).

104. A. A. Rifat, G. A. Mahdiraji, Y. M. Sua, Y. G. Shee, R. Ahmed, D. M. Chow, and F. R. M. Adikan, "Surface plasmon resonance photonic crystal fiber biosensor: a practical sensing approach," IEEE Photon. Technol. Lett. **27**, 1628–1631 (2015).

105. M. F. O. Hameed, Y. K. A. Alrayk, and S. S. A. Obayya, "Self-calibration highly sensitive photonic crystal fiber biosensor," IEEE Photon. J. **8**, 1–12 (2016).

106. N. Luan, R. Wang, W. Lv, and J. Yao, "Surface plasmon resonance sensor based on D-shaped microstructured optical fiber with hollow core," Opt. Express **23**, 8576–8582 (2015).

107. C. Zhou, Y. Zhang, L. Xia, and D. Liu, "Photonic crystal fiber sensor based on hybrid mechanisms: plasmonic and directional," Opt. Commun. **285**, 2466–2471 (2012).

108. G. An, S. Li, X. Yan, X. Zhang, Z. Yuan, H. Wang, Y. Zhang, X. Hao, Y. Shao, and Z. Hao, "Extra-broad photonic crystal fiber refractive index sensor based on surface plasmon resonance," Plasmonics **12**, 465–471(2016).

109. D. Gao, C. Guan, Y. Wen, X. Zhong, and L. Yuan, "Multi-hole fiber based surface plasmon resonance sensor operated at near-infrared wavelengths," Opt. Commun. **313**, 94–98 (2014).

110. M. Napiorkowski and W. Urbanczyk, "Effect of bending on surface plasmon resonance spectrum in microstructured optical fibers," Opt. Express **21**, 22762–22772 (2013).

111. M. Hautakorpi, M. Mattinen, and H. Ludvigsen, "Surface-plasmon-resonance sensor based on three-hole microstructured optical fiber," Opt. Express **16**, 8427–8432 (2008).

112. Y. Lu, C.-J. Hao, B.-Q. Wu, X.-H. Huang, W.-Q. Wen, X.-Y. Fu, and J.-Q. Yao, "Grapefruit fiber filled with silver nanowires surface plasmon resonance sensor in aqueous environments," Sensors **12**, 12016–12025 (2012).

113. X. Yang, Y. Lu, M. Wang, and J. Yao, "An exposed-core grapefruit fibers based surface plasmon resonance sensor," Sensors **15**, 17106–17114 (2015).

114. N. Luan and J. Yao, "Surface plasmon resonance sensor based on exposed-core microstructured optical fiber placed with a silver wire," IEEE Photon. J. **8**, 4800508 (2016).

115. C. J. Hao, Y. Lu, M. T. Wang, B. Q. Wu, L. C. Duan, and J. Q. Yao, "Surface plasmon resonance refractive index sensor based on active photonic crystal fiber," IEEE Photon. J. **5**, 4801108 (2013).

116. G. An, S. Li, W. Qin, W. Zhang, Z. Fan, and Y. Bao, "High-sensitivity refractive index sensor based on D-shaped photonic crystal fiber with rectangular lattice and nanoscale gold film," Plasmonics **9**, 1355–1360 (2014).

117. G. Wang, S. Li, G. An, X. Wang, Y. Zhao, W. Zhang, and H. Chen, "Highly sensitive D-shaped photonic crystal fiber biological sensors based on surface plasmon resonance," Opt. Quantum Electron. **48**, 46 (2016).

118. L. Peng, F. Shi, G. Zhou, S. Ge, Z. Hou, and C. Xia, "A surface plasmon biosensor based on a D-shaped microstructured optical fiber with rectangular lattice," IEEE Photon. J. **7**, 4801309 (2015).

119. Z. Tan, X. Hao, Y. Shao, Y. Chen, X. Li, and P. Fan, "Phase modulation and structural effects in a D-shaped all-solid photonic crystal fiber surface plasmon resonance sensor," Opt. Express **22**, 15049–15063 (2014).

120. F. Shi, L. Peng, G. Zhou, X. Cang, Z. Hou, and C. Xia, "An elliptical core D-shaped photonic crystal fiber-based plasmonic sensor at upper detection limit," Plasmonics **10**, 1263–1268 (2015).

121. J. N. Dash and R. Jha, "Highly sensitive D shaped PCF sensor based on SPR for near IR," Opt. Quantum Electron. **48**, 137 (2016).

122. J. N. Dash and R. Jha, "Highly sensitive side-polished birefringent PCF-based SPR sensor in near IR," Plasmonics **11**, 1505–1509(2016).

123. T. Huang, "Highly sensitive SPR sensor based on D-shaped photonic crystal fiber coated with indium tin oxide at near-infrared wavelength," Plasmonics, 1–6 (2016).

124. N. M. Y. Zhang, D. J. J. Hu, P. P. Shum, Z. Wu, K. Li, T. Huang, and L. Wei, "Design and analysis of surface plasmon resonance sensor based on high birefringent microstructured optical fiber," J. Opt. **18**, 065005 (2016).

125. X. Yu, S. Zhang, Y. Zhang, H.-P. Ho, P. Shum, H. Liu, and D. Liu, "An efficient approach for investigating surface plasmon resonance in asymmetric optical fibers based on birefringence analysis," Opt. Express **18**, 17950–17957 (2010).

126. C. Liu, F. Wang, S. Zheng, T. Sun, J. Lv, Q. Liu, L. Yang, H. Mu, and P. K. Chu, "Analysis of a highly birefringent asymmetric photonic crystal fibre based on a surface plasmon resonance sensor," J. Mod. Opt. **63**, 1189–1195 (2016).

127. S. Ge, F. Shi, G. Zhou, S. Liu, Z. Hou, and L. Peng, "U-shaped photonic crystal fiber based surface plasmon resonance sensors," Plasmonics **11**, 1307–1312 (2016).

128. J. N. Dash and R. Jha, "Graphene-based birefringent photonic crystal fiber sensor using surface plasmon resonance," IEEE Photon. Technol. Lett. **26**, 1092–1095 (2014).

129. J. N. Dash and R. Jha, "On the performance of graphene-based D-shaped photonic crystal fibre biosensor using surface plasmon resonance," Plasmonics **10**, 1123–1131 (2015).

130. A. A. Rifat, G. A. Mahdiragi, D. M. Chow, Y. G. Shee, R. Ahmed, and F. R. M. Adikan, "Photonic crystal fiber-based surface plasmon resonance sensor with selective analyte channels and graphene-silver deposited core," Sensors **15**, 11499–11510 (2015).

131. X. Yang, Y. Lu, B. Liu, and J. Yao, "Analysis of graphene-based photonic crystal fiber sensor using birefringence and surface plasmon resonance," Plasmonics **12**, 489–496 (2017).

132. A. A. Rifat, G. A. Mahdiraji, R. Ahmed, D. M. Chow, Y. M. Sua, Y. G. Shee, and F. R. M. Adikan, "Copper-graphene-based photonic crystal fiber plasmonics biosensor," IEEE Photon. J. **8**, 4800408 (2016).

133. Y. Zhang, L. Xia, C. Zhou, X. Yu, H. Liu, D. Liu, and Y. Zhang, "Microstructured fiber based plasmonic index sensor with optimized accuracy and calibration relation in large dynamic range," Opt. Commun. **284**, 4161–4166 (2011).

134. B. Shuai, L. Xia, Y. Zhang, and D. Liu, "A multi-core holey fiber based plasmonic sensor with large detection range and high linearity," Opt. Express **20**, 5974 (2012).

135. C. Liu, F. Wang, J. Lv, T. Sun, Q. Liu, H. Mu, and P. K. Chu, "Design and theoretical analysis of a photonic crystal fiber based on surface plasmon resonance sensing," J. Nanophoton. **9**, 093050 (2015).

136. B. Shuai, L. Xia, and D. Liu, "Coexistence of positive and negative refractive index sensitivity in the liquid-core photonic crystal fiber based plasmonic sensor," Opt. Express **20**, 25858–25866 (2012).

137. W. Qin, S. Li, Y. Yao, X. Xin, and J. Xue, "Analyte-filled core self-calibration microstructured optical fiber based plasmonic sensor for detecting high refractive index aqueous analyte," Opt. Laser Eng. **58**, 1–8 (2014).

138. M. S. A. Gandhi, S. Sivabalan, P. R. Babu, and K. Senthilnathan, "Designing a biosensor using a photonic quasi-crystal fiber," IEEE Sens. J. **16**, 2425–2430 (2016).

139. Z. Fan, S. Li, Q. Liu, G. An, H. Chen, J. Li, D. Chao, H. Li, J. Zi, and W. Tian, "High sensitivity of refractive index sensor based on analyte-filled photonic crystal fiber with surface plasmon resonance," IEEE Photon. J. **7**, 4800809 (2015).

140. Z. Tan, X. Li, Y. Chen, and P. Fan, "Improving the sensitivity of fiber surface plasmon resonance sensor by filling liquid in a hollow core photonic crystal fiber," Plasmonics **9**, 167–173 (2014).

141. B. Gauvreau, A. Hassani, M. F. Fehri, A. Kabashin, and M. Skorobogatiy, "Photonic bandgap fiber-based surface plasmon resonance sensors," Opt. Express **15**, 11413–11426 (2007).

142. A. Hassani, B. Gauvreau, M. F. Fehri, A. Kabashin, and M. Skorobogatiy, "Photonic crystal fiber and waveguide-based surface plasmon resonance sensors for application in the visible and near-IR," Electromagnetics **28**, 198–213 (2008).

143. M. Tian, P. Lu, L. Chen, C. Lv, and D. Liu, "All-solid D-shaped photonic fiber sensor based on surface plasmon resonance," Opt. Commun. **285**, 1550–1554 (2012).

144. Y. Zhang, C. Zhou, L. Xia, X. Yu, and D. Liu, "Wagon wheel fiber based multichannel plasmonic sensor," Opt. Express **19**, 22863–22873 (2011).

145. R. Otupiri, E. K. Akowuah, and S. Haxha, "Multi-channel SPR biosensor based on PCF for multi-analyte sensing applications," Opt. Express **23**, 15716–15727 (2015).

146. N. J. Florous, K. Saitoh, and M. Koshiba, "Numerical modeling of cryogenic temperature sensors based on plasmonic oscillations in metallic nanoparticles embedded into photonic crystal fibers," IEEE Photon. Technol. Lett. **19**, 324–326 (2007).

147. N. Luan, R. Wang, W. Lv, Y. Lu, and J. Yao, "Surface plasmon resonance temperature sensor based on photonic crystal fibers randomly filled with silver nanowires," Sensors **14**, 16035–16045 (2014).

148. M. Wang, Y. Lu, C. Hao, X. Yang, and J. Yao, "Simulation analysis of a temperature sensor based on photonic crystal fiber filled with different shapes of nanowires," Optik **126**, 3687–3691 (2015).

149. Y. Peng, J. Hou, Z. Huang, and Q. Li, "Temperature sensor based on surface plasmon resonance within selective coated photonic crystal fiber," Appl. Opt. **51**, 6361–6367 (2012).

150. Q. Liu, S. Li, H. Chen, J. Li, and Z. Fan, "High-sensitivity plasmonic temperature sensor based on photonic crystal fiber coated with nanoscale gold film," Appl. Phys. Express **8**, 046701 (2015).

151. D. Hu, J. Lim, Y. Cui, K. Milenko, Y. Wang, P. Shum, and T. Wolinski, "Fabrication and characterization of a highly temperature sensitive device based on nematic liquid crystal-filled photonic crystal fiber," IEEE Photon. J. **4**, 1248–1255 (2012).

152. D. Hu, P. Shum, Y. Cui, K. Milenko, Y. Wang, and T. Wolinski, "A compact and temperature-sensitive directional coupler based on photonic crystal fiber filled with liquid crystal 6CHBT," IEEE Photon. J. **4**, 2010–2016 (2012).

153. M. F. O. Hameed, M. Y. Azab, A. M. Heikal, S. M. El-Hefnawy, and S. S. A. Obayya, "Highly sensitive plasmonic photonic crystal temperature sensor filled with liquid crystal," IEEE Photon. Technol. Lett. **28**, 59–62 (2016).

154. N. Luan, C. Ding, and J. Yao, "A refractive index and temperature sensor based on surface plasmon resonance in an exposed-core microstructured optical fiber," IEEE Photon. J. **8**, 4801608 (2016).

155. J. Li, S. Wu, S. Brugioni, R. Meucci, and S. Faetti, "Infrared refractive indices of liquid crystals," J. Appl. Phys. **97**, 073501 (2005).

156. Y. Du, S.-G. Li, S. Liu, X.-P. Zhu, and X.-X. Zhang, "Polarization splitting filter characteristics of Au-filled high-birefringence photonic crystal fiber," Appl. Phys. B **109**, 65–74 (2012).

157. Z. Fan, S. Li, H. Chen, Q. Liu, W. Zhang, G. An, J. Li, and Y. Bao, "Numerical analysis of polarization filter characteristics of D-shaped photonic crystal fiber based on surface plasmon resonance," Plasmonics **10**, 675–680 (2015).

158. S. Yogalakshmi, S. Selvendran, and A. S. Raja, "Design and analysis of a photonic crystal fiber based polarization filter using surface plasmon resonance," Laser Phys. **26**, 056201 (2016).

159. F. Shi, G. Zhou, D. Li, L. Peng, Z. Hou, and C. Xia, "Surface plasmon mode coupling in photonic crystal fiber symmetrically filled with Ag/Au alloy wires," Plasmonics **10**, 335–340 (2015).

160. H. Chen, S. Li, M. Ma, J. Li, Z. Fan, and M. Shi, "Surface plasmon induced polarization filter based on Au wires and liquid crystal infiltrated photonic crystal fibers," Plasmonics **11**, 459–464 (2016).

161. M. F. O. Hameed, A. M. Heikal, B. M. Younis, M. Abdelrazzak, and S. S. A. Obayya, "Ultra-high tunable liquid crystal-plasmonic photonic crystal fiber polarization filter," Opt. Express **23**, 7007–7020 (2015).

162. Q. Liu, S. Li, J. Li, C. Dou, X. Wang, G. Wang, and M. Shi, "Tunable fiber polarization filter by filling different index liquids and gold wire into photonic crystal fiber," IEEE J. Lightwave Technol. **34**, 2484–2490 (2016).

163. W. Zhang, S. Li, G.-W. An, Z.-K. Fan, and Y.-J. Bao, "Polarization filter characteristics of photonic crystal fibers with square lattice and selectively filled gold wires," Appl. Opt. **53**, 2441–2445 (2014).

164. G. An, S. Li, X. Yan, Z. Yuan, and X. Zhang, "High-birefringence photonic crystal fiber polarization filter based on surface plasmon resonance," Appl. Opt. **55**, 1262–1266 (2016).

165. L.-H. Jiang, Y. Zheng, J.-J. Yang, L.-T. Hou, J.-Y. Peng, and X.-T. Zhang, "Design of an ultrashort single-polarization wavelength splitter based on gold-filled square-lattice photonic crystal fiber," Opt. Quantum Electron. **48**, 409 (2016).

166. L. Jiang, Y. Zheng, J. Yang, L. Hou, Z. Li, and X. Zhao, "An ultra-broadband single polarization filter based on plasmonic photonic crystal fiber with a liquid crystal core," Plasmonics **12**, 411–417 (2017).

167. A. M. Heikal, F. F. K. Hussain, M. F. O. Hameed, and S. S. A. Obayya, "Efficient polarization filter design based on plasmonic photonic crystal fiber," J. Lightwave Technol. **33**, 2868–2875 (2015).

168. S. Zhang, X. Yu, Y. Zhang, P. Shum, Y. Zhang, L. Xia, and D. Liu, "Theoretical study of dual-core photonic crystal fibers with metal wire," IEEE Photon. J. **4**, 1178–1187 (2012).

169. P. Li and J. Zhao, "Polarization-dependent coupling in gold-filled dual-core photonic crystal fibers," Opt. Express **21**, 5232–5238 (2013).

170. B. Sun, M.-Y. Chen, J. Zhou, and Y.-K. Zhang, "Surface plasmon induced polarization splitting based on dual core photonic crystal fiber with metal wire," Plasmonics **8**, 1253–1258 (2013).

171. B. Sun, M.-Y. Chen, Y.-K. Zhang, and J. Zhou, "Polarization-dependent coupling characteristics of metal-wire filled dual-core photonic crystal fiber," Opt. Quantum Electron. **47**, 441–451 (2015).

172. A. Khaleque, E. G. Mironov, and H. T. Hattori, "Analysis of the properties of a dual-core plasmonic photonic crystal fiber polarization splitter," Appl. Phys. B **121**, 523–532 (2015).

173. A. Khaleque and H. T. Hattori, "Ultra-broadband and compact polarization splitter based on gold filled dual-core photonic crystal fiber," J. Appl. Phys. **118**, 143101 (2015).

174. Z. Fan, S. Li, Q. Liu, H. Chen, and X. Wang, "Plasmonic broadband polarization splitter based on dual-core photonic crystal fiber with elliptical metallic nanowires," Plasmonics **11**, 1565–1572 (2016).

175. Q. Liu, S. Li, Z.-K. Fan, W. Zhang, H. Li, J.-C. Zi, and G.-W. An, "Numerical analysis of ultrabroadband polarization splitter based on gold-filled dual-core photonic crystal fiber," Opt. Commun. **334**, 46–50 (2015).

176. L. Jiang, Y. Zheng, L. Hou, K. Zheng, J. Peng, and X. Zhao, "An ultrabroadband polarization splitter based on square-lattice dual-core photonic crystal fiber with a gold wire," Opt. Commun. **351**, 50–56 (2015).

177. M. F. O. Hameed, R. T. Balat, A. M. Heikal, M. M. Abo-Elkhier, M. I. A. E. Maaty, and S. S. A. Obayya, "Polarization-independent surface plasmon liquid crystal photonic crystal multiplexer-demultiplexer," IEEE Photon. J. **7**, 4801110 (2015).

178. L. Chen, W. Zhang, Q. Zhou, Y. Liu, J. Sieg, Y. Zhang, L. Wang, B. Wang, and T. Yan, "Polarization rotator based on hybrid plasmonics photonic crystal fiber," IEEE Photon. Technol. Lett. **26**, 2291–2294 (2014).

179. C. Dou, X. Jing, S. Li, Q. Liu, and J. Bian, "A photonic crystal fiber polarized filter at 1.55 μm based on surface plasmon resonance," Plasmonics **11**, 1163–1168 (2015).

180. X. Hao, S. Li, X. Yan, X. Zhang, G. An, H. Wang, Y. Shao, and Z. Han, "Photonic crystal fibre polarization filter with round lattice based on surface plasmon resonance," J. Modern Opt. **64**, 205–209 (2017).

181. G. Wang, S. Li, G. An, X. Wang, and Y. Zhao, "Design of a polarization filtering photonic crystal fiber with a big gold-coated air hole," Opt. Quantum Electron. **48**, 457 (2016).

182. L. Jiang, Y. Zheng, L. Hou, K. Zheng, and J. Peng, "Surface plasmon induced polarization filter of the gold-coated photonic crystal fiber with a liquid core," Opt. Fiber Technol. **23**, 42–47 (2015).

183. J. Xue, S. Li, Y. Xiao, W. Qin, X. Xin, and X. Zhu, "Polarization filter characters of the gold-coated and the liquid filled photonic crystal fiber based on surface plasmon resonance," Opt. Express **21**, 13733–13740 (2013).

184. X. Wang, S. Li, H. Chen, Q. Liu, G. Wang, and Y. Zhao, "Compatibility of temperature sensor and polarization filter based on Au film and glycerin selectively infilling photonic crystal fibers," Plasmonics **11**, 1265–1271 (2016).

185. Q. Liu, S. Li, and H. Chen, "Two kinds of polarization filter based on photonic crystal fiber with nanoscale gold film," IEEE Photon. J. **7**, 2700210 (2015).

186. G. Wang, S. Li, X. Wang, Y. Zhao, Q. Liu, J. Zi, H. Li, and H. Chen, "A kind of broadband polarization filter based on photonic crystal fiber with nanoscale gold film," Plasmonics **12**, 377–382 (2017).

187. Y. Han, L. Xia, Y.-T. Zhang, and W. Li, "Ultra-broad band single-polarization single-mode photonic crystal fiber based on the zero-order surface plasmon polariton mode," Opt. Commun. **345**, 141–148 (2015).

188. H. Chen, S. Li, M. Ma, Z. Fan, and Y. Wu, "Ultrabroad bandwidth polarization filter based on D-shaped photonic crystal fibers with gold film," Plasmonics **10**, 1239–1242 (2015).

189. H. Chen, S. Li, G. An, J. Li, Z. Fan, and Y. Han, "Polarization splitter based on D-shaped dual-core photonic crystal fibers with gold film," Plasmonics **10**, 57–61 (2015).

190. Z. Fan, S. Li, Q. Liu, J. Li, and Y. Xie, "Plasmonic polarization beam splitter based on dual-core photonic crystal fiber," Plasmonics **10**, 1283–1289 (2015).

191. L. Chen, W. Zhang, Z. Zhang, Y. Liu, J. Sieg, L. Zhang, Q. Zhou, L. Wang, B. Wang, and T. Yan, "Design for a single-polarization photonic crystal fiber wavelength splitter based on hybrid-surface plasmon resonance," IEEE Photon. J. **6**, 2200909 (2014).

192. Q. Liu, S. Li, J. Li, H. Chen, Z. Fan, G. An, H. Li, and J. Zi, "Photonic crystal fiber polarization filter based on coupling between core mode and SPP mode," Plasmonics **11**, 857–863 (2016).

193. G. Wang, S. Li, G. An, X. Wang, Y. Zhao, and W. Zhang, "Design of a polarized filtering photonic-crystal fiber with gold-coated air holes," Appl. Opt. **54**, 8817–8820 (2015).

194. J. Zi, S. Li, W. Zhang, and G. An, "Polarization filter characteristics of square lattice photonic crystal fiber with a large diameter gold-coated air hole," Plasmonics **10**, 1499–1504 (2015).

195. J. Zi, S. Li, H. Chen, J. Li, and H. Li, "Photonic crystal fiber polarization filter based on surface plasmon polaritons," Plasmonics **11**, 65–69 (2016).

196. Q. Liu, S. Li, H. Li, J. Zi, W. Zhang, Z. Fan, G. An, and Y. Bao, "Broadband single-polarization photonic crystal fiber based on surface plasmon resonance for polarization filter," Plasmonics **10**, 931–939 (2015).

197. A. Khaleque and H. T. Hattori, "Polarizer based upon a plasmonic resonant thin layer on a squeezed photonic crystal fiber," Appl. Opt. **54**, 2543–2549 (2015).

198. H. Li, S. Li, H. Chen, J. Li, G. An, and J. Zi, "A polarization filter based on photonic crystal fiber with asymmetry around gold-coated holes," Plasmonics **11**, 103–108 (2016).

199. D. Poudereux, M. Caño-García, J. F. Algorri, B. García-Cámara, J. M. Sánchez-Pena, X. Quintana, M. A. Geday, and J. M. Otón, "Thermally tunable polarization by nanoparticle plasmonic resonance in photonic crystal fibers," Opt. Express **23**, 28935–28944 (2015).

200. S. Bose, R. Chattopadhyay, S. Roy, and S. K. Bhadra, "Study of nonlinear dynamics in silver-nanoparticle-doped photonic crystal fiber," J. Opt. Soc. Am. B **33**, 1014–1021 (2016).

201. M. Sadeghi, V. Ahmadi, and M. Ebnali-Heidari, "Metal-coated silicon nanowire embedded plasmonic photonic crystal fiber: Kerr nonlinearity and two-photon absorption," Plasmonics, 1–9 (2016).

202. A. Tuniz, B. T. Kuhlmey, P. Y. Chen, and S. C. Fleming, "Weaving the invisible thread: design of an optically invisible metamaterial fibre," Opt. Express **18**, 18095–18105 (2010).

Dr. Dora Juan Juan Hu received her B.Eng (1st Hon.) and Ph.D. degree from the school of Electrical and Electronic Engineering, Nanyang Technological University, Singapore in 2004 and 2010, respectively. She joined the RF & Optical Department, Institute for Infocomm Research, Agency for Science, Technology and Research (A*STAR), Singapore from 2009 to 2012 to develop novel fiber devices for sensor applications. In 2012 she received an A*STAR post-doctoral fellowship (2012–2014). In 2012 she joined the Wellman Center for Photomedicine, Massachusetts General Hospital, Boston, Massachusetts, as a research fellow and worked on novel photonic technologies for endoscopic diagnosis. Dora joined the Femtosecond Optics Group, Imperial College London, in August 2013 and worked on visible and mid-infrared fiber lasers. She is now with the Smart Energy and Environment Cluster, Institute for Infocomm Research, A*STAR, Singapore and is working on developing photonic solutions for smart infrastructure and the healthcare industry.

Ho Pui Ho received his B.Eng and Ph.D. in Electrical and Electronic Engineering from the University of Nottingham in 1986 and 1990, respectively. Currently a professor in the Department of Electronic Engineering, The Chinese University of Hong Kong (CUHK), he has held positions as Associate Dean of Engineering, CUHK; Assistant Professor in the Department of Physics and Materials Science, City University of Hong Kong; and Senior Process Engineer for semiconductor laser fabrication at Hewlett-Packard. He started as a compound semiconductor materials scientist, and his current academic interests focus on nano-sized semiconductor materials for photonic and sensor applications, optical instrumentation, surface plasmon resonance biosensors, lab-on-a-chip, and biophotonics. He has published over 300 peer-reviewed articles and 16 Chinese and six U.S. patents. He is a Fellow of SPIE and HKIE and a senior member of IEEE.